# Ultrasound Elastography Using Multiple Images

Hassan Rivaz, Emad M. Boctor, Michael A. Choti, Gregory D. Hager

*Department of Computer Science*
*Johns Hopkins University*
*Baltimore, MD, USA*

**Abstract**

Displacement estimation is an essential step for ultrasound elastography and numerous techniques have been proposed to improve its quality using *two* frames of ultrasound RF data. This paper introduces a technique for calculating a displacement field from *three (or multiple)* frames of ultrasound RF data. To calculate a displacement field using three images, we first derive constraints on variations of the displacement field with time using mechanics of materials. These constraints are then used to generate a regularized cost function that incorporates amplitude similarity of three ultrasound images and displacement continuity. We optimize the cost function in an expectation maximization (EM) framework. Iteratively reweighted least squares (IRLS) is used to minimize the effect of outliers. An alternative approach for utilizing multiple images is to only consider two frames at any time and sequentially calculate the strains, which are then accumulated. We formally show that, compared to using two images or accumulating strains, the new algorithm reduces the noise and eliminates ambiguities in displacement estimation. The displacement field is used to generate strain images for quasi-static elastography. Simulation, phantom experiments and *in-vivo* patient trials of imaging liver tumors and monitoring ablation therapy of liver cancer are presented for validation. We show that even with the challenging patient data, where it is likely to have one frame among the three that is not optimal for strain estimation, the introduction of physics-based prior as well as the simultaneous consideration of three images significantly improves the quality of strain images. Average values for strain images of two frames versus ElastMI are: 43 versus 73 for SNR (signal to noise ratio) in simulation data, 11 versus 15 for CNR (contrast to noise ratio) in phantom data, and 5.7 versus 7.3 for CNR in patient data. In addition, the improvement of ElastMI over both utilizing two images and accumulating strains is statistically significant in the patient data, with $p$-values of respectively 0.006 and 0.012.

*Keywords:* Ultrasound Elastography, Elasticity Imaging, Strain Imaging, Ablation, Liver, Hepatocellular Carcinoma, HCC, Expectation Maximization, EM, Physics-Based Priors

## 1. Introduction

Displacement or time delay estimation in ultrasound images is an essential step in numerous medical imaging tasks including the rapidly growing field of imaging the mechanical properties of tissue (Ophir et al., 1999; Greenleaf et al., 2003; Parker et al., 2005). In this work, we perform displacement estimation for quasi-static ultrasound elastography (Ophir et al., 1999), which involves deforming the tissue slowly with an external mechanical force and imaging the tissue during the deformation. More specifically, we focus on real-time freehand palpation elastography (Hall et al., 2003; Hiltawsky et al., 2001; Doyley et al., 2001; Yamakawa et al., 2003; Zahiri and Salcudean, 2006; Deprez et al., 2009; Goenezen et al., 2012) where the external force is applied by simply pressing the ultrasound probe against the tissue. Ease of use, real-time performance and providing invaluable elasticity images for diagnosis and guidance/monitoring of surgical operations are invaluable features of freehand palpation elastography.

A typical ultrasound frame rate is 20-60 fps. As a result, an entire series of ultrasound images are freely available during the tissue deformation. Multiple ultrasound images have been used before to obtain strain images of highly compressed tissue by accumulating the intermediate strain images (O'Donnell et al., 1994; Varghese et al., 1996; Lubinski et al., 1999) and to obtain persistently high quality strain images by performing weighted averaging of the strain images (Hiltawsky et al., 2001; Jiang et al., 2007, 2006; Chen et al., 2010; Foroughi et al., 2010). Accumulating and averaging strain images increases their signal to noise ratio (SNR) and contrast to noise ratio (CNR) (calculated according to equation 35). However, these techniques are susceptible to drift, a problem with any sequential tracking system. We show that considering three images simultaneously to solve for displacement field significantly improves the quality of the elasticity images compared to sequentially accumulating them. Multiple images have also been used to obtain tissue non-linear parameters (Krouskop et al., 1998; Erkamp et al., 2004a; Oberai et al., 2009; Goenezen et al., 2012).

Depth calculation from a trinocular-stereo system (Ayache

*Email addresses:* rivaz@jhu.edu (Hassan Rivaz), eboctor1@jhmi.edu (Emad M. Boctor), michael.choti@utsouthwestern.edu (Michael A. Choti), hager@cs.jhu.edu (Gregory D. Hager)
*URL:* http://cs.jhu.edu/~rivaz/ (Hassan Rivaz)

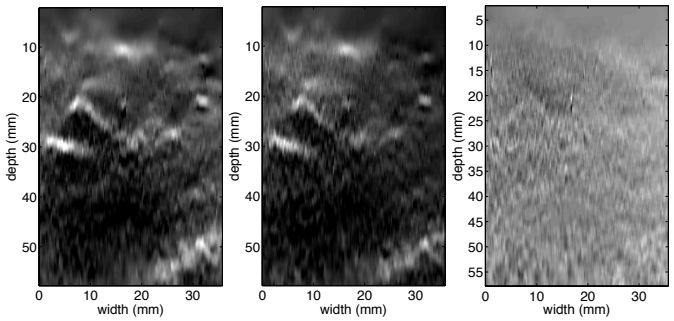


Figure 1: Consecutive strain images are "similar" up to a scale factor. First and second ($S_1$ and $S_2$ from left) are two strain fields calculated from $I_1$ and $I_2$, and from $I_2$ and $I_3$ respectively ($I_1$, $I_2$ and $I_3$ not shown here). $S_1$ & $S_2$ look similar. Third image is $S_1 - \eta S_2$ for $\eta = 1.1$. The strain range in the first two images is 0 to 0.6%, and in the third image is ±0.3%. Images are acquired freehand and *in-vivo* during liver surgery.

and Lustman, 1991; Mulligan et al., 2002; Brown et al., 2003) is a similar problem where more than two images are used to increase the accuracy and robustness of the stereo system. The third image is used to introduce additional geometric constraints and to reduce the noise in the depth estimates. Unfortunately, these geometric constraints do not hold in the elastography paradigm, and therefore these methods cannot be applied to elastography.

Figure 1 shows *two consecutive strain images* calculated from *three ultrasound images* using the 2D analytic minimization (AM) method (Rivaz et al., 2011a)[1]. Our motivation is to utilize the similarity of these two images to calculate a low variance displacement field from three images. We derive physical constraints based on the mechanical properties of soft tissue, and incorporate them into a novel algorithm that we call ElastMI (Elastography using Multiple Images). ElastMI minimizes a cost function that incorporates data obtained from three images and exploits the mechanical constraints. Like Pellot-Barakat et al. (2004); Jiang and Hall (2006); Sumi (2008); Sumi and Sato (2008); Brusseau et al. (2008); Rivaz et al. (2008a, 2009, 2011a); McCormick et al. (2011), we use a regularized cost function that exploits tissue motion continuity to reduce the variance of the displacement estimates caused by ultrasound signal decorrelations. The cost function is optimized using an iterative algorithm based on expectation maximization (EM) (Moon, 1996). Compared to our previous work (Rivaz et al., 2011b), we present significantly more details and in-depth analysis of ElastMI. We also provide extensive results for validation and more analysis of the results.

To formally study the advantage of using three images, we assume ultrasound noise is additive Gaussian and prove that exploiting three images not only reduces the noise in the displacement estimation, but also eliminates false matches due to possible periodic patterns in the tissue. We assume an additive Gaussian noise model in ultrasound images for two main reasons. First, most real-time motion estimation techniques use different forms of sum of squared differences (SSD) as a similarity metric. This includes window-based methods [2] and the sample based methods of 2D AM and ElastMI. The fact that these similarity metrics have been shown to give low noise displacement estimates suggests that additive Gaussian noise model is a good approximation for the true ultrasonic noise for small deformations. Second, using the additive Gaussian noise model in ultrasound images allows us to analytically obtain the noise in the estimated displacement field as a function of the image noise for three different algorithms: AM (Rivaz et al., 2011a), ElastMI, and a third method that we propose in the Appendix.

We use simulation, phantom and *in-vivo* patient trials to validate our results. The *in-vivo* patient trials that we present in this work are related to imaging liver tumors and also imaging ablation lesions generated by thermal ablation. Thermal ablation is a less invasive alternative for tumor resection where the cancer tumor is coagulated at temperatures above 60° Celsius. To eliminate cancer recurrence, the necrosis should cover the entire tumor in addition to some safety margin around it. Currently, both guidance and monitoring of ablation are performed under ultrasound visualization. Unfortunately, many cancer tumors in liver have similar echogenicity to normal tissue and are not discernible in ultrasound images. Regarding ablation monitoring, the hyperechoic region in the ultrasound image caused by formation of gas bubbles during ablation does not represent tissue ablation and usually disappears within 1 hour of ablation (Goldberg et al., 2000). To minimize the misclassification of these hyperechoic regions with ablated lesion, ultrasound elastography has been proposed for monitoring ablation: HIFU probes (high intensity focused ultrasound) (Righetti et al., 1999), radio-frequency Cool-tip probes (Valleylab/Tyco Healthcare Group, Boulder, CO) (Fahey et al., 2006; Jiang and Varghese, 2009; Jiang et al., 2010) and radio-frequency RITA probes (Rita Medical Systems, Fremont, CA) (Varghese et al., 2003, 2004; Boctor et al., 2004; Rivaz et al., 2008b) have been investigated. Electrode vibration elastography (Bharat et al., 2008; DeWall et al., 2012a) and shear wave imaging (Arnal et al., 2011) have also been used to monitor ablation. Elastography in the presence of gas bubbles is challenging because they are a major source of noise in the ultrasound signal and degrade the quality of both B-mode and strain images.The noise associated to them is also not simply additive Gaussian and depends strongly on both the spatial location and time. We show that ElastMI generates high quality strain images in such high noise environment in three patient trials.

The contributions of this work are: (1) introducing constraints on variation of the motion fields based on similarities of strain images through *time*; (2) proposing ElastMI, an EM-based algorithm to solve for motion fields using three images; (3) formally proving that the ElastMI algorithm reduces displacement estimation variance, and further illustrating that with simulation, phantom and patient data, and (4) reporting clinical

[1] The 2D AM code is available online at `www.cs.jhu.edu/~rivaz`

[2] Real-time window based methods generally use SSD, cross correlation or normalized cross correlation as the similarity metric. Under certain normality conditions, it can be shown that all of these methods are maximum likelihood estimators if the ultrasound noise model can be assumed to be additive Gaussian.

studies of ablation guidance/monitoring, with data collection corresponding to before, during and after ablation, which is to the best of our knowledge, the first such study.

## 2. Displacement Estimation Error

Assume we have a set of ultrasound frames $J_k$, $k = 1 \cdots p$, each of size $m \times n$, and let $\mathbf{x} = (i, j)$, $i = 1 \cdots m$, $j = 1 \cdots n$ be a 2D vector denoting the coordinates of image samples (Figure 2). The images are obtained during the freehand palpation of the tissue. From the original sequence $J_k$, we pick a triple, and set $I_1$ as the middle image, and $I_2$ and $I_3$ as the first and third images. Let $\tilde{\boldsymbol{d}}^k(\mathbf{x}) = (\tilde{a}^k(\mathbf{x}), \tilde{l}^k(\mathbf{x}))$ denote the ground truth axial and lateral displacements of the sample $\mathbf{x}$ between the 1st and $k^{\text{th}}$ image (see Figure 2). Note that, by choice of reference, $\tilde{\boldsymbol{d}}^1(\mathbf{x}) = 0$. For simplicity, we only look at a particular A-line and also assume that the motion $\tilde{\boldsymbol{d}}^k$ is in the axial direction. Therefore, $\tilde{a}_i^k$, $i = 1 \cdots m$ denote the ground truth axial displacement of samples of the particular A-line. The subscript $i$ shows the dependency of $\tilde{a}^k$ to $\mathbf{x}$. Assuming that ultrasound noise is additive Gaussian, the image intensity at point $i$ is

$$I_k(i) = \tilde{I}(i - \tilde{a}_i^k) + n_k(i), \;\; n_k(i) \sim \mathcal{N}(0, \sigma^2), \;\; k = 1 \cdots p \quad (1)$$

where $\mathcal{N}(\mu, \sigma^2)$ denotes a Gaussian distribution with the mean $\mu$ and variance $\sigma^2$, and $\tilde{I}(i)$ refers to an unknown ideal image that has no noise and no deformation. The goal of ElastMI is to estimate $\tilde{a}_i^k$, i.e. a displacement for *every* sample. We make two comparisons between ElastMI and companding (Chaturvedi et al., 1998): (1) in companding, the scaling of the signal is directly computed and can be used as a strain image, while ElastMI does not directly estimate scaling. (2) ElastMI allows the signal to be stretched since it allows every sample to have a different displacement. Therefore, like companding methods it can give accurate results for images with large displacements.

In Rivaz et al. (2011a), we proposed the following cost function for calculating the displacement field between $I_1$ and $I_k$:

$$\begin{aligned} C(a_1^k \cdots a_m^k) &= C_D + C_R, \\ C_D &= \sum_{i=1}^{m} \left(I_1(i) - I_k(i + a_i^k)\right)^2, \\ C_R &= \sum_{i=2}^{m} \left(a_i^k - a_{i-1}^k\right)^2 \end{aligned} \quad (2)$$

where $C_D$ and $C_R$ are respectively the data and regularization terms. We have assumed pure axial motion. Replacing $I_1$ and $I_k$ with $\tilde{I}$ from equation 1 we have

$$C_D(a_1^k \cdots a_m^k) = \sum_{i=1}^{m} \left(\tilde{I}(i) - \tilde{I}(i + a_i^k - \tilde{a}_i^k) + n_1(i) - n_k(i + a_i^k)\right)^2 \quad (3)$$

Using Taylor series to linearize $\tilde{I}(i + a_i^k - \tilde{a}_i^k)$ around $i$ we have

$$C_D(a_1^k \cdots a_m^k) = \sum_{i=1}^{m} \left(-(a_i^k - \tilde{a}_i^k)^T \cdot \tilde{I}'_a(i) + n_1(i) - n_k(i + a_i^k)\right)^2 \quad (4)$$

where $\tilde{I}'_a$ is the derivative of the image in the axial direction (subscript $a$ indicates that the derivative is performed in the axial direction). The value of $a_i^k$ that minimizes $C_D$ can be easily found by setting the $\partial C_D / \partial a_i^k$ to zero:

$$a_i^k = \tilde{a}_i^k - \left[\tilde{I}'_a(i)\right]^{-1} \left(n_1(i) - n_k(i + a_i^k)\right) \quad (5)$$

where $[\cdot]^{-1}$ denotes inversion. The expected value and variance of the $a_i^k$ are therefore

$$\mathbb{E}[a_i^k] = \tilde{a}_i^k \quad (6)$$

$$var[a_i^k] = \left[\tilde{I}'_a(i)\right]^{-2} var[n_1(i) - n_k(i + a_i^k)] = 2\sigma^2 \left[\tilde{I}'_a(i)\right]^{-2} \quad (7)$$

where $\sigma^2$ is the noise in the images as presented in equation 1. These equations show that without regularization, the expected value of the displacement is the true displacement (i.e. there is no bias), and its variance increases with image noise $\sigma$. The variance decreases where image gradient is high, i.e. at the tissue boundaries and areas where speckle is present. This is why speckle tracking methods do not work (i.e. have very high estimation variance) in cysts, which do not have speckle.

We now investigate the redundancy in consecutive strain images by looking at the mechanics of the tissue. We then introduce new priors into our displacement estimation technique based on this redundancy.

## 3. Deriving Physical-Based Constraints

In this Section, we assume quasi-static motion and derive constraints on the variations of the tissue displacement with time. We use these constraints in the ElastMI algorithm, Section 4, to decrease the error in the displacement estimation.

To calculate the deformations of a continuum, mechanical characteristics of the continuum and the external forces (i.e. boundary conditions) are required. The mechanical characteristics of a continuum itself can be described by the three properties of *stress-strain relationship (linear or nonlinear), homogeneity* and *isotropy*. Linear stress-strain behavior means that if we scale the stress (or force) by a factor, the strain (or displacement) also gets scaled by the same factor, i.e. the Hooke's law. The stress-strain relation is linear for a large range ordinary objects. Many tissue types also display linear stress-strain relation in the 0 to 5% strain range (Emelianov et al., 1998; Yeh et al., 2002; Greenleaf et al., 2003; Erkamp et al., 2004a,b; Hall et al., 2007, 2009; Oberai et al., 2009). Homogeneity means that the continuum has uniform mechanical properties, i.e. its properties are spatially invariant. Isotropy means that at each point, the continuum has the same properties in different directions. Muscle for example is not an isotropic material due to its fibers. For simplicity and for intuitive analysis, we only consider scalar fields and ignore anisotropy. We can therefore analyze how a continuum deforms by selecting one of these three properties: linear or non-linear continuum, homogeneous or inhomogeneous continuum, and external forces that result in uniform stress or nonuniform stress (resulting in $2^3 = 8$ cases).

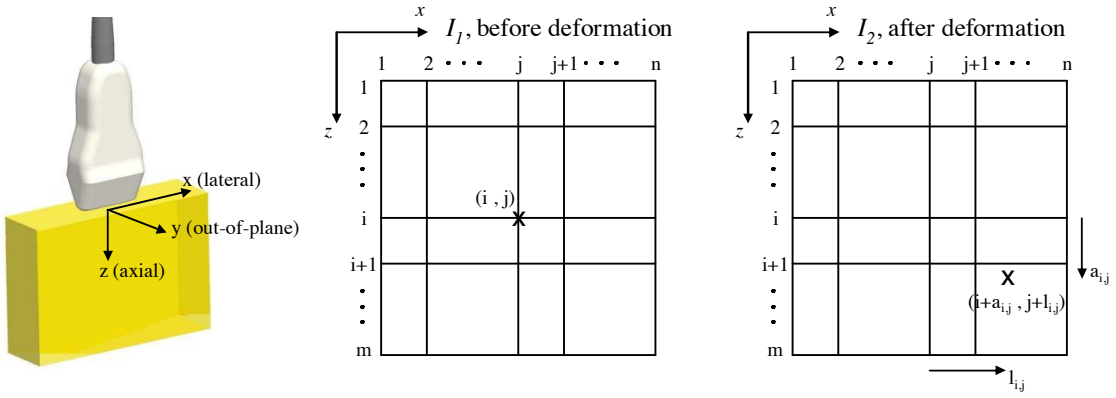


Figure 2: Axial, lateral and out-of-plane directions. The coordinate system is attached to the ultrasound probe. The sample (i,j) marked by x moved by $(a_{i,j}, l_{i,j})$.

We hypothesize that the ratio of two strain (or displacement) images obtained at different times from the same continuum has small spatial variations (as observed in Figure 1). To illustrate this, we show that among the 8 total cases, this ratio is spatially invariant in the five cases shown in Figure 3. The remaining three cases all share tissue non-linearity, which we avoid by limiting the total strain to less than 5%. In this figure, image $I_1$ is acquired at zero compression (to simplify the figure), image $I_2$ after compression and image $I_3$ after more compression. We assume the applied pressure in $I_2$ and $I_3$ has the same profile (i.e. the two external pressure fields are the same up to a scale factor). This means that in cases (a), (c) and (e) the applied pressure is always uniform and in (b) and (d) the applied pressure has the same profile. $P_1$ and $P_2$ are two arbitrary points whose strain values are $\epsilon_1^k$ and $\epsilon_2^k$ and whose axial displacement values are $a_1^k$ and $a_2^k$ respectively, where $k = 2, 3$ refers to strain value at image $k$. We prove that in the five cases shown in Figure 3 , the ratio of the strain images and the ratio of the displacement images are spatially invariant, i.e.

$$\frac{\epsilon_1^2}{\epsilon_1^3} = \frac{\epsilon_2^2}{\epsilon_2^3} \quad \text{and} \quad \frac{a_1^2}{a_1^3} = \frac{a_2^2}{a_2^3}. \tag{8}$$

An intuitive proof for this equation in the five cases shown in Figure 3 is as following:

**(a)** Linear, homogeneous, uniform stress. This is the simplest case, and equation 8 can be proven because $\epsilon_1^2 = \epsilon_2^2$ and $\epsilon_1^3 = \epsilon_2^3$ (since the stress is uniform). The second part $\frac{a_1^2}{a_1^3} = \frac{a_2^2}{a_2^3}$ can also be simply proven by noticing that two triangles $OZ_1P_1^2$ and $OZ_2P_2^2$, as well as the two triangles $OZ_1P_1^3$ and $OZ_2P_2^3$ are similar.

**(b)** Linear, homogeneous, **non-uniform stress**. Either the hole in the continuum or the non-uniform force applied to the top is enough to generate non uniform stress and strain fields. This case might be the hardest to prove equation 8. Consider the finite element analysis of the continuum, which meshes the continuum into small parts. Since the continuum is linear, the final force-displacement equation becomes $\mathbf{f} = K\mathbf{a}$ where $\mathbf{f}$ is the force vector applied to the boundaries, $K$ is the stiffness matrix and $\mathbf{a}$ is the displacement of each node in the mesh. Let the forces when $I_2$ and $I_3$ are acquired be respectively $\mathbf{f}^2$ and $\mathbf{f}^3$, and the displacements be respectively $\mathbf{a}^2$ and $\mathbf{a}^3$. Since we have assumed the pressure keeps its profile, $\mathbf{f}^2$ and $\mathbf{f}^3$ are identical up to a scale, i.e. $\mathbf{f}^2 = \eta\mathbf{f}^3$. Using $\mathbf{f} = K\mathbf{a}$, we have $\mathbf{a}^2 = \eta\mathbf{a}^3$ and therefore the second part of equation 8. Since the displacements are scaled version of each other, so are the strains and therefore we have the first part of equation 8.

**(c)** Linear, **inhomogeneous**, uniform stress. Because of linearity and uniform stress, $s^2 = E_1\epsilon_1^2 = E_2\epsilon_2^2$ and $s^3 = E_1\epsilon_1^3 = E_2\epsilon_2^3$ ($s^2$ and $s^3$ are the stress values corresponding respectively to $I_2$ and $I_3$ and are not related to $s^2$ which is variance elsewhere in the paper). Dividing two equations gives equation 8. The second part $\frac{a_1^2}{a_1^3} = \frac{a_2^2}{a_2^3}$ can be proven as following. Because both parts are linear, it can be shown that the extension of the two curves corresponding to the bottom part of the image (the dashed lines) intersect at $a = 0$ axis (if linearity is not met, they do not intersect on $a = 0$ axis). Therefore, it can be shown that $\frac{a_1^2}{a_1^3} = \frac{a_2^2}{a_2^3}$ holds exploiting similarity relationships between the six triangles generated in the displacement-depth curve. If linearity is not held, neither part of equation 8 holds.

**(d)** Linear, **inhomogeneous**, **non-uniform stress**. Since the tissue is linear, this case can be proven by superposition using cases (b) and (c).

**(e)** **Non-linear**, homogeneous, uniform stress. The proof is the same as case (a) where linearity was not used.

Our analysis in (c) and (d) can be simply extended to an inhomogeneous medium with $n$ homogeneous parts, which is a good approximation for most inhomogeneous tissues. Although we assumed only axial displacement and strain, equation 8 can be similarly proven for 2D strain and stress in the above five cases. For the remaining $8 - 5 = 3$ cases equation 8 does not hold even in the 1D case. In addition, other simplifications such as assuming strain and stress to be scalars (rather than tensors), neglecting anisotropic behavior of tissue, assuming that

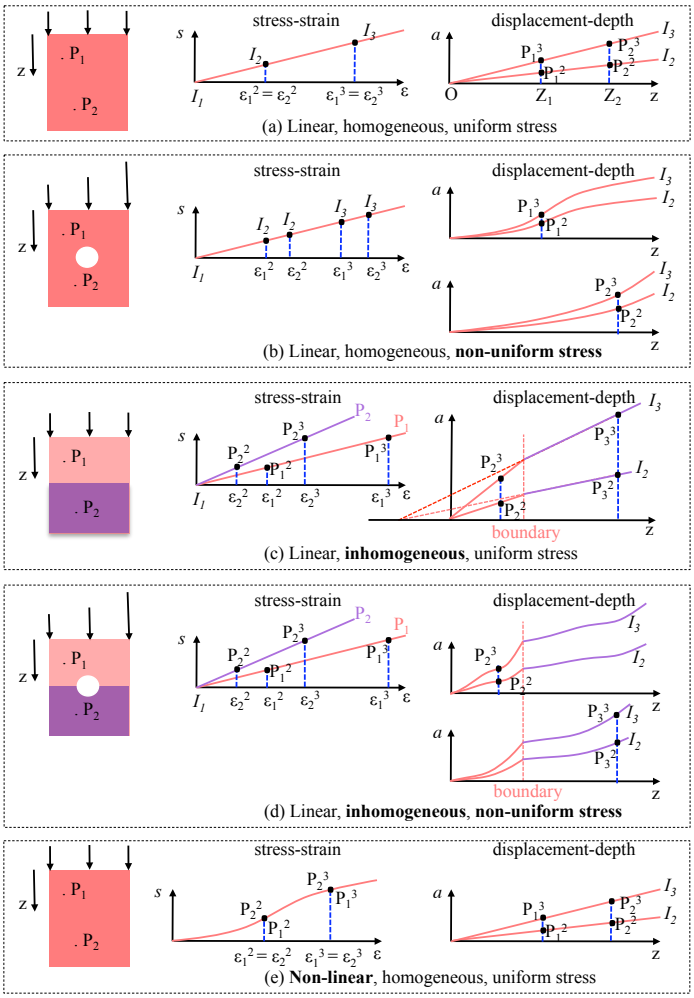


Figure 3: Five cases for which equation 8 holds (i.e. different strain or displacement images are simply scaled version of each other). $s$, $\epsilon$, $a$ and z are respectively stress, strain, axial displacement and axial direction as before. Refer to the text for details.

the pressure profile does not change from $I_2$ to $I_3$, and biological motions inside the living tissue limit the scope of equation 8. However many tissue types (linear or nonlinear, homogeneous or inhomogeneous and isotropic or anisotropic) combined with any applied pressure can be locally approximated with one of the above cases. Therefore, we impose the additional constraint that *the ratio between two displacement fields should have limited spatial variations* (instead of the more rigorous constraint that it should be spatially invariant). Let $\eta_i$ (which has small spatial variations) be the scaling factor at each sample $i$: $a_i^3 = \eta_i a_i^2$. In the 2D case, the scale factor is $\boldsymbol{\eta}_i$ where $\mathbf{d}_i^3 = \boldsymbol{\eta}_i . * \mathbf{d}_i^2$ where $.*$ denotes element-wise multiplication[3]. In the next Section, we present the algorithm that utilizes this constraint.

[3] Axial and lateral strains are related through the Poisson's ratio $\nu$. For now we simply assume they are independent and hence we use the point-wise operation. In Section 4 we take the relation between the axial and lateral strains into account.

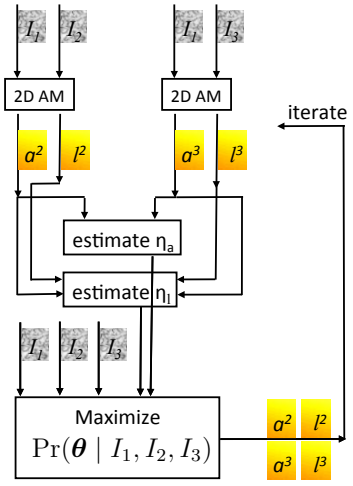


Figure 4: The ElastMI algorithm. The reference image $I_1$ corresponds to an intermediate deformation between $I_2$ and $I_3$.

## 4. ElastMI: Elastography using Multiple Images

We have a set of $p = 3$ images $I_k$, $k = 1 \cdots 3$, and would like to calculate the two 2D displacement fields $\mathbf{d}^2 = (a^2, l^2)$ and $\mathbf{d}^3 = (a^3, l^3)$ as described in the beginning of Section 2. We assume $\mathbf{d}^3 = \boldsymbol{\eta} . * \mathbf{d}^2$ where $\boldsymbol{\eta} = (\eta_a, \eta_l)$ and $\eta_a$ and $\eta_l$ are the ratios between respectively the axial and lateral displacement images. Following the discussion in Section 3, $\mathbf{d}^2$ and $\mathbf{d}^3$ have to result in strain values of less than 5% so that the tissue can be approximately linear. In a freehand palpation elastography setup with ultrasound acquisition rate of 20 fps or more, taking three consecutive images as $I_2$, $I_1$, $I_3$ guarantees this.

Let $\boldsymbol{\theta}$ contain all the displacement unknowns $\mathbf{d}^2$ and $\mathbf{d}^3$. If we know $\boldsymbol{\eta}$, it is relatively easy to estimate $\boldsymbol{\theta}$ by maximizing its posterior probability. On the other hand, it is easy to estimate $\boldsymbol{\eta}$ if we have $\boldsymbol{\theta}$. Since we know neither, we iterate between the steps of estimating $\boldsymbol{\theta}$ and $\boldsymbol{\eta}$ using an Expectation Maximization (EM) framework. Our proposed algorithm, shown in Figure 4, is as follows.

1. Find an estimate for $\boldsymbol{\theta}$ by applying the 2D AM method (Rivaz et al., 2011a) to two pairs of images ($I_1$,$I_2$) and ($I_1$,$I_3$) independently.
2. Find an estimate for $\boldsymbol{\eta}$ using the calculated $\boldsymbol{\theta}$ (details below).
3. Using the estimated $\boldsymbol{\eta}$, estimate $\boldsymbol{\theta}$ by maximizing its posterior probability (details below). Note that unlike the traditional EM where the likelihood of $\boldsymbol{\theta}$ is maximized, we maximize its posterior probability.
4. Iterate between 2 and 3 until convergence.

Different stopping criteria can be used in step 4, such as terminating the iteration when the changes in the displacement field or the cost function is smaller than a predefined threshold. We found that the convergence of the ElastMI algorithm is fast and iterating it only once always generates strain images with high quality and CNR; we therefore use this simple criteria. Steps 2 and 3 are elaborated below.

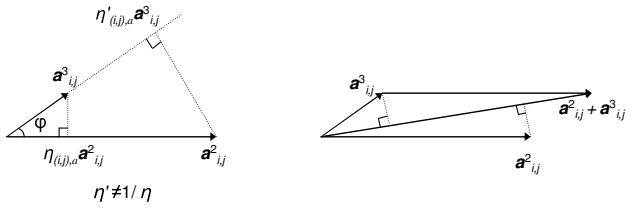


Figure 5: Calculating the scale factor $\eta$ from two strain images $\mathbf{a}^2$ and $\mathbf{a}^3$. Left shows how the calculation of $\eta$ through equation 10 is not symmetric. It is trivial to show that $\eta'_{(i,j),a} = 1/\eta_{(i,j),a}$ holds if and only if $\varphi = 0$ or $\varphi = \pi$, a condition that is not generally guaranteed. Right shows a symmetric approach for calculating $\eta$ where both vectors are projected into $\mathbf{a}^2_{i,j} + \mathbf{a}^3_{i,j}$. The ratio of the two projections is a symmetric measure for $\eta$ (equation 11).

**Calculating $\eta$ from $\theta$ using least squares:** At each sample $(i, j)$ in the displacement field $\mathbf{d}^2_{i,j}$, $i = 1 \cdots m$, $j = 1 \cdots n$ take a window of size $m_w \times n_w$ centered at the sample ($m_w$ and $n_w$ are in the axial and lateral directions respectively and both are odd numbers). Stack the axial and lateral components of $\mathbf{d}^2_{i,j}$ that are in the window in two vectors $\mathbf{a}^2_{i,j}$ and $\mathbf{l}^2_{i,j}$, each of length $m_w \times n_w$. Similarly, generate $\mathbf{a}^3_{i,j}$ and $\mathbf{l}^3_{i,j}$ using $\mathbf{d}^3$. Note that since both displacement fields $\mathbf{d}^2_{i,j}$ and $\mathbf{d}^3_{i,j}$ are calculated with respect to samples on $I_1$, the displacements correspond to the same sample $(i, j)$. We first calculate the axial component $\eta_{(i,j),a}$ ($\boldsymbol{\eta}_{(i,j)} = (\eta_{(i,j),a}, \eta_{(i,j),l})$). Discarding the spatial information in $\mathbf{a}^2_{i,j}$ and $\mathbf{a}^3_{i,j}$, we can average the two vectors into two scalers $\bar{\mathbf{a}}^2_{i,j}$ and $\bar{\mathbf{a}}^3_{i,j}$ and simply calculate $\eta_{(i,j),a} = \bar{\mathbf{a}}^3_{i,j}/\bar{\mathbf{a}}^2_{i,j}$. However, a more elegant way which also takes into account the spatial information is by calculating the least squares solution to the following over-determined problem

$$\mathbf{a}^2_{i,j}\eta_{(i,j),a} = \mathbf{a}^3_{i,j} \tag{9}$$

which results in

$$\eta_{(i,j),a} = \frac{\mathbf{a}^{2T}_{i,j}\mathbf{a}^3_{i,j}}{\mathbf{a}^{2T}_{i,j}\mathbf{a}^2_{i,j}} \tag{10}$$

where superscript $T$ denotes transpose. This is however not symmetric w.r.t. $\mathbf{a}^2_{i,j}$ and $\mathbf{a}^3_{i,j}$: if we define $\eta'_{(i,j),a}$ to be the least square solution to $\mathbf{a}^3_{i,j}\eta'_{(i,j),a} = \mathbf{a}^2_{i,j}$, it is easy to show $\eta'_{(i,j),a} \neq 1/\eta_{(i,j),a}$ (Figure 5). A method for symmetric calculation of $\eta$ is depicted in Figure 5 where both vectors are projected into $\mathbf{a}^2_{i,j} + \mathbf{a}^3_{i,j}$. The ratio of the two projections is $\eta$, i.e.

$$\eta_{(i,j),a} = \frac{\mathbf{a}^{3T}_{i,j}(\mathbf{a}^2_{i,j} + \mathbf{a}^3_{i,j})}{\mathbf{a}^{2T}_{i,j}(\mathbf{a}^2_{i,j} + \mathbf{a}^3_{i,j})} \tag{11}$$

To calculate the ratio of the lateral displacement fields $\eta_{(i,j),l}$, we take into account possible lateral slip of the probe, which results in a rigid-body-motion. The rigid-body-motion can be simply calculated by averaging the lateral displacement in $\mathbf{d}^2_{i,j}$ and $\mathbf{d}^3_{i,j}$ in the entire image $i = 1 \cdots m$, $j = 1 \cdots n$, and then calculating the difference between these two average lateral displacements. The lateral scaling factor $\eta_{(i,j),l}$ can be calculated using an equation similar to 11 where the axial displacement $\mathbf{a}_{i,j}$ is replaced with the lateral displacements $\mathbf{l}_{i,j}$. However, we use the following approach which results in a better estimate for $\eta_{(i,j),l}$. The lateral strain $\epsilon_l$ (the gradient of the lateral displacement in the lateral direction) is simply $\nu\epsilon_a$ where $\nu$ is an unknown Poisson's ratio. Since $\nu$ has a small dynamic range in soft tissue (Konofagou and Ophir, 1998) and since the difference between the two displacement maps $\mathbf{d}^2$ and $\mathbf{d}^3$ is small, we can assume that $\nu$ does not vary from $\mathbf{d}^2$ to $\mathbf{d}^3$. Therefore, $\eta_{(i,j),l} = \eta_{(i,j),a}$. This gives better estimate for $\eta_{(i,j),l}$ since axial displacement estimation is more accurate (Rivaz et al., 2011a).

**Calculating $\theta$ by maximizing its posterior probability.** Knowing the value of the latent variable $\boldsymbol{\eta}$, the posterior probability of $\boldsymbol{\theta}$ can be written as

$$\Pr(\boldsymbol{\theta} \mid I_1, I_2, I_3) \propto \Pr(I_1, I_2, I_3 \mid \boldsymbol{\theta}, \eta) \Pr(\boldsymbol{\theta} \mid \eta) \tag{12}$$

where we have ignored the normalization denominator. The data term $\Pr(I_1, I_2, I_3 \mid \boldsymbol{\theta}, \eta)$ is the likelihood of $\boldsymbol{\theta}$ parameters $L(\boldsymbol{\theta} \mid I_1, I_2, I_3, \eta)$. We set the prior term $\Pr(\boldsymbol{\theta} \mid \eta)$ to a regularization $R(\boldsymbol{\theta} \mid \eta)$. The MAP estimate for $\boldsymbol{\theta}$ is

$$\boldsymbol{\theta}_{MAP} = \arg\max_{\boldsymbol{\theta}} \Pr(\boldsymbol{\theta} \mid I_1, I_2, I_3). \tag{13}$$

To be able to solve this equation analytically, we assume all the samples in the three images are independent and identically distributed and that their noise is Gaussian (equation 1). The likelihood of $\boldsymbol{\theta}$ can therefore be simply written as the product of Gaussian random variables:

$$L(\boldsymbol{\theta} \mid I_1, I_2, I_3, \eta) = \prod_{i=1}^{m} \frac{1}{\sqrt{2\pi\sigma^2}} \exp(-\frac{(I_1(\mathbf{x}_i) - I_2(\mathbf{x}_i + \mathbf{d}^2_i))^2}{2\sigma^2}) \cdot$$

$$\prod_{i=1}^{m} \frac{1}{\sqrt{2\pi\sigma^2}} \exp(-\frac{(I_1(\mathbf{x}_i) - I_3(\mathbf{x}_i + \mathbf{d}^3_i))^2}{2\sigma^2}) \tag{14}$$

Note that we are calculating the displacements of the vertical columns (RF-line samples) simultaneously and therefore the multiplication is performed from 1 to $m$. $\mathbf{d}^3_i$ can be replaced by $\boldsymbol{\eta}_i \cdot * \mathbf{d}^2_i$. Since the prior $\Pr(\boldsymbol{\theta} \mid \boldsymbol{\eta})$ and the likelihood function are multiplied in the posterior probability (equation 12), we set the regularization to be Gaussian so that the posterior probability can be easily minimized:

$$\Pr(\boldsymbol{\theta} \mid \boldsymbol{\eta}) = \prod_{i=1}^{m} \frac{1}{2\pi\,|A|^{1/2}} \exp[-(\mathbf{d}^2_i - \mathbf{d}^2_{i-1})^T A (\mathbf{d}^2_i - \mathbf{d}^2_{i-1})],$$

$$A = diag(\alpha(\boldsymbol{\eta}, \varphi), \beta(\boldsymbol{\eta}, \varphi)) \tag{15}$$

where $A$ is a 2x2 diagonal matrix as indicated, $|\cdot|$ denotes the determinant operator and $\alpha$ and $\beta$ are the axial and lateral regularization weights. $\alpha$ and $\beta$ can be dependent on $\boldsymbol{\eta}$ and also on the angle $\varphi$ between $\mathbf{a}^3_{i,j}$ and $\mathbf{a}^2_{i,j}$ (Figure 5), but in this work we simply set them to constant values. Inserting equations 14 and 15 into equation 12 and taking its log followed by negation, we arrive at the cost function

$$C(\boldsymbol{\theta}) = -\log \Pr(\boldsymbol{\theta} \mid I_1, I_2, I_3) = \sum_{i=1}^{m} (I_1(\mathbf{x}_i) - I_2(\mathbf{x}_i + \mathbf{d}^2_i))^2 +$$

$$\sum_{i=1}^{m}(I_1(\mathbf{x}_i)-I_3(\mathbf{x}_i+\boldsymbol{\eta}_i.*\mathbf{d}_i^2))^2+\sum_{i=1}^{m}(\mathbf{d}_i^2-\mathbf{d}_{i-1}^2)^T A(\mathbf{d}_i^2-\mathbf{d}_{i-1}^2)+f(A,\sigma^2) \tag{16}$$

where $f(A,\sigma^2)$ contains all the terms that do not have $\mathbf{d}$ and therefore can be ignored in finding the optimum $\mathbf{d}$ value. We can now linearize $I_2(\mathbf{x}_i+\mathbf{d}_i^2)$ and $I_3(\mathbf{x}_i+\boldsymbol{\eta}_i.*\mathbf{d}_i^2)$ respectively around $\mathbf{x}_i+\mathbf{d}_i^{AM}$ and $\mathbf{x}_i+\boldsymbol{\eta}_i.*\mathbf{d}_i^{AM}$ where $\mathbf{d}_i^{AM}$ is an estimate value for $\mathbf{d}_i^2$, known by comparing $I_1$ and $I_2$ using 2D AM. This approach, however, is not symmetric and does not take $\mathbf{d}^3$ into account as the initial estimate (although $\mathbf{d}^3$ is used to estimate $\boldsymbol{\eta}$). A symmetric initial estimate for $\mathbf{d}_i^2$ and $\mathbf{d}_i^3$ is

$$\hat{\mathbf{d}}_i^2=\frac{\eta_{i,a}\mathbf{d}_i^2+\mathbf{d}_i^3}{2\eta_{i,a}},\ \hat{\mathbf{d}}_i^3=\frac{\eta_{i,a}\mathbf{d}_i^2+\mathbf{d}_i^3}{2}=\eta_{i,a}\hat{\mathbf{d}}_i^2. \tag{17}$$

Note that we have only used $\eta_{i,a}$ since we have assumed $\eta_{i,l}=\eta_{i,a}$. We have also dropped the subscript $j$ since the cost function $C$ is defined for a specific A-line at each time. Taylor expansion can now be used to linearize $I_2(\mathbf{x}_i+\mathbf{d}_i^2)$ and $I_3(\mathbf{x}_i+\boldsymbol{\eta}_i.*\mathbf{d}_i^2)$ in equation 16 respectively around $\hat{\mathbf{d}}_i^2$ around $\hat{\mathbf{d}}_i^3$ :

$$\begin{aligned}C(\boldsymbol{\theta})=&\sum_{i=1}^{m}\left(I_1(\mathbf{x}_i)-I_2(\mathbf{x}_i+\hat{\mathbf{d}}_i^2)-\Delta\mathbf{d}_i^{2T}\nabla I_2(\mathbf{x}_i+\hat{\mathbf{d}}_i^2)\right)^2\\&+\sum_{i=1}^{m}\left(I_1(\mathbf{x}_i)-I_3(\mathbf{x}_i+\eta_{i,a}\hat{\mathbf{d}}_i^2)-\eta_{i,a}\Delta\mathbf{d}_i^{2T}\nabla I_3(\mathbf{x}_i+\eta_{i,a}\hat{\mathbf{d}}_i^2)\right)^2\\&+\sum_{i=1}^{m}(\mathbf{d}_i^2-\mathbf{d}_{i-1}^2)^T A(\mathbf{d}_i^2-\mathbf{d}_{i-1}^2)+f(A,\sigma^2)\end{aligned} \tag{18}$$

where $\Delta\mathbf{d}_i^2=\mathbf{d}_i^2-\hat{\mathbf{d}}_i^2$. Setting the derivative of $C$ w.r.t. the axial ($\Delta a_i^2=\Delta\mathbf{d}_{i,a}^2$) and lateral ($\Delta l_i^2=\Delta\mathbf{d}_{i,l}^2$) components of $\Delta\mathbf{d}_i^2$ for $i=1\cdots m$ to zero and stacking the $2m$ unknowns in $\Delta\mathbf{d}^2=\left[\Delta a_1^2\ \Delta l_1^2\ \Delta a_2^2\ \Delta l_2^2\cdots\Delta a_m^2\ \Delta l_m^2\right]^T$ and the $2m$ initial estimates in $\hat{\mathbf{d}}^2=\left[\hat{a}_1^2\ \hat{l}_1^2\ \hat{a}_2^2\ \hat{l}_2^2\cdots\hat{a}_m^2\ \hat{l}_m^2\right]^T$ we obtain the linear system of size $2m$:

$$(\mathscr{I}'+\mathscr{D})\Delta\mathbf{d}^2=\boldsymbol{r}-\mathscr{D}\hat{\mathbf{d}}^2,$$

$$\mathscr{D}=\begin{bmatrix}\alpha&0&-\alpha&0&0&0&\cdots&0\\0&\beta&0&-\beta&0&0&\cdots&0\\-\alpha&0&2\alpha&0&-\alpha&0&\cdots&0\\0&-\beta&0&2\beta&0&-\beta&\cdots&0\\0&0&-\alpha&0&2\alpha&0&\cdots&0\\\vdots&&&&&&\ddots&\\0&0&0&\cdots&-\alpha&0&\alpha&0\\0&0&0&\cdots&0&-\beta&0&\beta\end{bmatrix}, \tag{19}$$

where $\mathscr{I}'$ is a symmetric tridiagonal matrix of size $2m\times 2m$ with $2\times 2$ matrices $\mathfrak{I}'$ in its diagonal:

$$\mathscr{I}'=diag(\mathfrak{I}'^2(1)\cdots\mathfrak{I}'^2(m)),$$

$$\mathfrak{I}'^2(i)=\begin{bmatrix}{I'_{2,a}}^2+\eta_{i,a}{}^2{I'_{3,a}}^2&I'_{2,a}I'_{2,l}+\eta_{i,a}\eta_{i,l}I'_{3,a}I'_{3,l}\\I'_{2,a}I'_{2,l}+\eta_{i,a}\eta_{i,l}I'_{3,a}I'_{3,l}&{I'_{2,l}}^2+\eta_{i,l}{}^2{I'_{3,l}}^2\end{bmatrix} \tag{20}$$

where $I'_2$ and $I'_3$ are calculated respectively at $(\mathbf{x}_i+\hat{\mathbf{d}}_i^2)$ and at $(\mathbf{x}_i+\boldsymbol{\eta}_i.*\hat{\mathbf{d}}_i^2)$, superscript $'$ indicates derivative and subscript $a$ and $l$ determine whether the derivation is in the axial or lateral direction, and $\boldsymbol{r}$ is a vector of length $2m$ with elements:

$$\begin{aligned}i\text{ odd}:\ r_i=&I'_{2,a}(\mathbf{x}_i+\hat{\mathbf{d}}_i^2)\left[I_1(\mathbf{x}_i)-I_2(\mathbf{x}_i+\hat{\mathbf{d}}_i^2)\right]+\\&\boldsymbol{\eta}_i.*I'_{3,a}(\mathbf{x}_i+\boldsymbol{\eta}_i.*\hat{\mathbf{d}}_i^2)\left[I_1(\mathbf{x}_i)-I_3(\mathbf{x}_i+\boldsymbol{\eta}_i.*\hat{\mathbf{d}}_i^2)\right]\\i\text{ even}:\ r_i=&I'_{2,l}(\mathbf{x}_i+\hat{\mathbf{d}}_i^2)\left[I_1(\mathbf{x}_i)-I_2(\mathbf{x}_i+\hat{\mathbf{d}}_i^2)\right]+\\&\boldsymbol{\eta}_i.*I'_{3,l}(\mathbf{x}_i+\boldsymbol{\eta}_i.*\hat{\mathbf{d}}_i^2)\left[I_1(\mathbf{x}_i)-I_3(\mathbf{x}_i+\boldsymbol{\eta}_i.*\hat{\mathbf{d}}_i^2)\right]\end{aligned} \tag{21}$$

The inverse gradient estimation method Rivaz et al. (2011a) can be used to make the method more computationally efficient: all the derivatives of $I_2$ at $(\mathbf{x}_i+\hat{\mathbf{d}}_i^2)$ and derivatives of $I_3$ at $(\mathbf{x}_i+\boldsymbol{\eta}_i.*\hat{\mathbf{d}}_i^2)$ will be simply replaced with the derivatives of $I_1$ at $\mathbf{x}_i$. With this modification, equation 20 becomes

$$\mathfrak{I}'^2(i)=\begin{bmatrix}(1+\eta_{i,a}{}^2){I'_{1,a}}^2&(1+\eta_{i,a}\eta_{i,l})I'_{1,a}I'_{1,l}\\(1+\eta_{i,a}\eta_{i,l})I'_{1,a}I'_{1,l}&(1+\eta_{i,l}{}^2){I'_{1,l}}^2\end{bmatrix}$$

and equation 21 becomes

$$\begin{aligned}i\text{ even}:\ r_i&=I'_{1,a}(\mathbf{x}_i)\left[I_1(\mathbf{x}_i)-I_2(\mathbf{x}_i+\hat{\mathbf{d}}_i^2)\right]+\\&\quad\boldsymbol{\eta}_i.*I'_{1,a}(\mathbf{x}_i)\left[I_1(\mathbf{x}_i)-I_3(\mathbf{x}_i+\boldsymbol{\eta}_i.*\hat{\mathbf{d}}_i^2)\right]\\i\text{ odd}:\ r_i&=I'_{1,l}(\mathbf{x}_i)\left[I_1(\mathbf{x}_i)-I_2(\mathbf{x}_i+\hat{\mathbf{d}}_i^2)\right]+\\&\quad\boldsymbol{\eta}_i.*I'_{1,l}(\mathbf{x}_i)\left[I_1(\mathbf{x}_i)-I_3(\mathbf{x}_i+\boldsymbol{\eta}_i.*\hat{\mathbf{d}}_i^2)\right]\end{aligned} \tag{22}$$

We minimize the effect of outliers via iterative reweighted least squares (IRLS) by giving a small weight to the outliers. Each image pair in equation 18 is checked independently, i.e. for the same sample $i$, two different weights $w_{12,i}$ and $w_{13,i}$ are used:

$$\begin{aligned}C(\boldsymbol{\theta})=&\sum_{i=1}^{m}w_{12,i}\left(I_1(\mathbf{x}_i)-I_2(\mathbf{x}_i+\hat{\mathbf{d}}_i^2)-\Delta\mathbf{d}_i^{2T}\nabla I_2(\mathbf{x}_i+\hat{\mathbf{d}}_i^2)\right)^2\\&+\sum_{i=1}^{m}w_{13,i}\left(I_1(\mathbf{x}_i)-I_3(\mathbf{x}_i+\eta_{i,a}\hat{\mathbf{d}}_i^2)-\eta_{i,a}\Delta\mathbf{d}_i^{2T}\nabla I_3(\mathbf{x}_i+\eta_{i,a}\hat{\mathbf{d}}_i^2)\right)^2\\&+\sum_{i=1}^{m}(\mathbf{d}_i^2-\mathbf{d}_{i-1}^2)^T A(\mathbf{d}_i^2-\mathbf{d}_{i-1}^2)+f(A,\sigma^2)\end{aligned} \tag{23}$$

where $w_{12}$ and $w_{13}$ are Huber (Hager and Belhumeur, 1998; Huber, 1997) weights and are calculated as:

$$\begin{aligned}w_{12,i}&=w(I_1(\mathbf{x}_i)-I_2(\mathbf{x}_i+\hat{\mathbf{d}}_i^2))\\w_{13,i}&=w(I_1(\mathbf{x}_i)-I_3(\mathbf{x}_i+\eta_{i,a}\hat{\mathbf{d}}_i^2))\\w(r_i)&=\begin{cases}1&|r_i|<T\\\frac{T}{|r_i|}&|r_i|>T\end{cases}\end{aligned} \tag{24}$$

where $T$ is a tunable parameter which determines the residual

level for which the sample can be treated as outlier. A small $T$ will treat many samples as outliers. With these new weights, equation 19 still holds with the following modifications:

$$\mathfrak{I}'^2(i) = \begin{bmatrix} (w_{12,i} + w_{13,i}\eta_{i,a}{}^2){I'_{1,a}}^2 & (w_{12,i} + w_{13,i}\eta_{i,a}\eta_{i,l})I'_{1,a}I'_{1,l} \\ (w_{12,i} + w_{13,i}\eta_{i,a}\eta_{i,l})I'_{1,a}I'_{1,l} & (w_{12,i} + w_{13,i}\eta_{i,l}{}^2){I'_{1,l}}^2 \end{bmatrix} \tag{25}$$

and equation 21 becomes

$$\begin{aligned} i \text{ even}: \; r_i =& w_{12,i}I'_{1,a}(\mathbf{x}_i)\left[I_1(\mathbf{x}_i) - I_2(\mathbf{x}_i + \hat{\mathbf{d}}_i^2)\right] + \\ & w_{13,i}\boldsymbol{\eta}_i. * I'_{1,a}(\mathbf{x}_i)\left[I_1(\mathbf{x}_i) - I_3(\mathbf{x}_i + \boldsymbol{\eta}_i. * \hat{\mathbf{d}}_i^2)\right] \\ i \text{ odd}: \; r_i =& w_{12,i}I'_{1,l}(\mathbf{x}_i)\left[I_1(\mathbf{x}_i) - I_2(\mathbf{x}_i + \hat{\mathbf{d}}_i^2)\right] + \\ & w_{13,i}\boldsymbol{\eta}_i. * I'_{1,l}(\mathbf{x}_i)\left[I_1(\mathbf{x}_i) - I_3(\mathbf{x}_i + \boldsymbol{\eta}_i. * \hat{\mathbf{d}}_i^2)\right]. \end{aligned} \tag{26}$$

To obtain a displacement field from three images using the ElastMI algorithm, equation 19 -with parameters defined in equations 25 and 26- is solved.

In the next two Sections we show that exploiting the third image reduces displacement variance and eliminates ambiguity.

### *4.1. Reducing Variance in Displacement Estimation*

Similar to Section 2, we assume the motion is only in the axial direction. Adding the similarity metric between images 1 and 2 and 1 and 3 we have

$$\begin{aligned} C_D(a_1^2 \cdots a_m^2,\ \eta_1 \cdots \eta_m) =& \sum_{i=1}^{m}\left(I_1(i) - I_2(i + a_i^2)\right)^2 \\ &+ \sum_{i=1}^{m}\left(I_1(i) - I_3(i + \eta_i a_i^2)\right)^2 \end{aligned} \tag{27}$$

and using the noise model of equation 1 we arrive at

$$\begin{aligned} & C_D(a_1^2 \cdots a_m^2,\ \eta_1 \cdots \eta_m) = \\ & \sum_{i=1}^{m}\left(\tilde{I}(i) - \tilde{I}(i + a_i^2 - \tilde{a}_i^2) + n_1(i) - n_2(i + a_i^2)\right)^2 + \\ & \sum_{i=1}^{m}\left(\tilde{I}(i) - \tilde{I}(i + \eta_i a_i^2 - \eta_i\tilde{a}_i^2) + n_1(i) - n_3(i + \eta_i a_i^2)\right)^2. \end{aligned} \tag{28}$$

The displacement can now be estimated by linearizing $\tilde{I}(i + a_i^2 - \tilde{a}_i^2)$ and $\tilde{I}(i + \eta_i a_i^2 - \eta_i\tilde{a}_i^2)$ around $i$ and minimizing $C_D$:

$$a_i^2 = \tilde{a}_i^2 - \left[\tilde{I}'_a(i)\right]^{-1}\frac{-(\eta_i + 1)n_1(i) + n_2(i + a_i^3) + \eta_i n_3(i + a_i^3)}{\eta^2 + 1} \tag{29}$$

and therefore

$$\mathbb{E}[a_i^2] = \tilde{a}_i^2 \tag{30}$$

$$var[a_i^2] = \sigma^2\left[\tilde{I}'_a(i)\right]^{-2}\frac{(\eta_i + 1)^2 + \eta_i^2 + 1}{(\eta_i^2 + 1)^2}. \tag{31}$$

Let's consider a case where $\eta_i = -1$, which indicates that the deformation from $I_1$ to $I_2$ is equal to the negative of the deformation from $I_1$ to $I_3$ (i.e. one is compression and the other one is extension) . Setting $\eta = -1$ we have $var[a_i^2] = 0.5\sigma^2\left[\nabla\tilde{I}\right]^{-2}$, which is $1/4^{th}$ of the $var[a_i^2]$ when only two images are utilized (equation 7). This reduction in the noise is a result of using three images and also incorporating the prior that the displacement fields at different instances of the tissue deformation are not independent. Please note that in our formulation all images are compared to image 1, so that ElastMI formulation can be extended to more than 3 images. However, in our implementation we compare images with the middle image, i.e. we compare $I_1$ with $I_2$, and $I_2$ with $I_3$. Therefore, since the ultrasound frame rate is much higher than the hand-held palpation frequency, $\eta_i$ is negative.

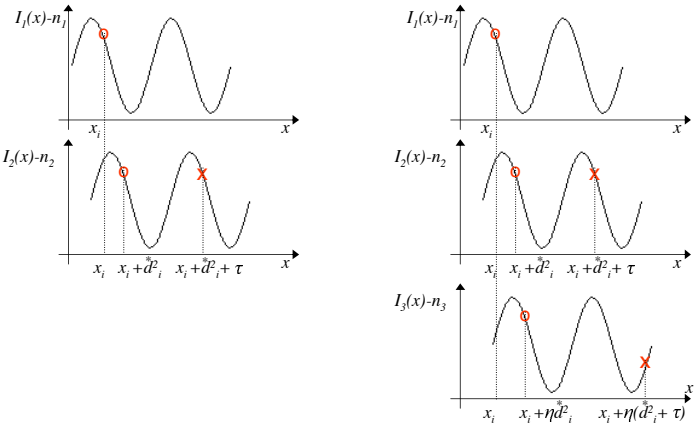


Figure 6: Eliminating ambiguity with three images. Left shows that it is impossible with two images to differentiate true displacement from false displacement when the underlying ultrasound image is periodic. The O and X marks can both be the match of the O in the top image. Right shows the addition of the third image (in the bottom) disambiguates the false displacement from the true displacement. Here, the X cannot be the match anymore since in the third image it corresponds to a different intensity value. $\eta$ is approximately 1.5.

It is important to note that this equation does not provide an exact comparison between ElastMI and AM. It assumes zero regularization, while the regularization terms in both AM and ElastMI methods significantly reduce the displacement estimation variance.

By way of comparison, we propose a method in the Appendix for calculating *two* displacement fields from *three* ultrasound RF data frames. Unlike ElastMI, this method does not impose constraints based on mechanics of materials. Instead, it uses natural constraints among the three displacement fields defined by the three images. We show that this method does not decrease the variance of displacement estimation.

### *4.2. Eliminating Ambiguity in Displacement Estimation*

Ambiguity has been reported before as a source of large errors in the displacement estimation (Hall et al., 2003; Viola and Walker, 2005). Periodic ultrasound patterns happen if the tissue scatterers are organized regularly on a scale comparable to ultrasound wavelength, such as the lobules of the liver and the portal triads (Fellingham and Sommer, 1983; Varghese et al., 1994). We show that an ambiguity in displacement estimation using two images can be resolved with three images. Assume

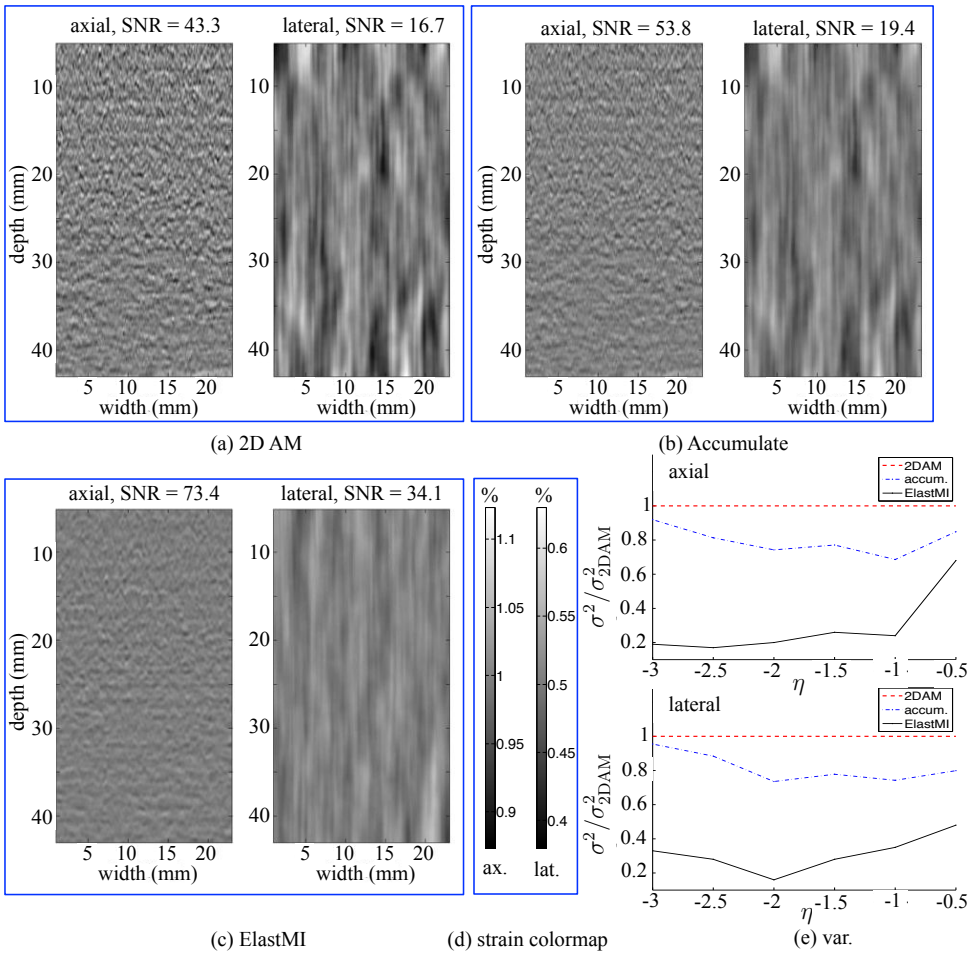


Figure 8: Strain results of the simulated images of Figure 7. (a) to (c) show the axial and lateral strain images, with color-maps shown in (d). In (a) only F7 and F8 are used, while in (b) and (c) three frames of F5, F7 and F8 are utilized. (e) shows the ratio of the variance of the strain of different methods compared to 2D AM with different $\eta$ values. Accumulating strains and ElastMI both give lower than 1 ratios. ElastMI gives the smallest variance.

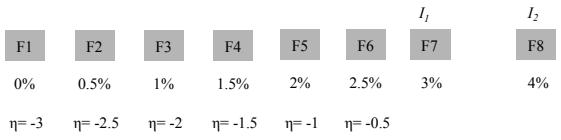


Figure 7: 8 simulated ultrasound image frames of a uniform phantom. The percentile under each frame shows the value of the compression w.r.t. $F_1$. We set $I_1$ and $I_2$ to $F_7$ and $F_8$ as shown and one of F1 to F6 frames as $I_3$, resulting in different $\eta$ values shown at the bottom. Note that we set the reference image $I_1$ such that its deformation is between $I_2$ and $I_3$.

that the ground truth image $\tilde{I}$ of equation 1 has the same intensity at $i$ and at $i+\tau$, i.e.

$$I_k(i) = \tilde{I}(i - \tilde{a}_i^k) + n_k(i), \quad k = 1,2,3, \quad \tilde{I}(i) = \tilde{I}(i+\tau) \tag{32}$$

where $n_k(i)$ is Gaussian noise as defined in equation 1. Equation 3 now can be written as

$$C_D = \sum_{i=1}^{m} \left(\tilde{I}(i) - \tilde{I}(i+\tau+a_i^k-\tilde{a}_i^k-\tau) + n_1(i) - n_k(i+a_i^k)\right)^2 \tag{33}$$

where we have added and subtracted $\tau$ to the argument of $\tilde{I}(i + a_i^k - \tilde{a}_i^k)$. Now it can be seen that $C_D$ has two local minima at $a_i^k = \tilde{a}_i^k$ and at $a_i^k = \tilde{a}_i^k + \tau$. In addition, the expected value of $C_D$ at both local minima is equal:

$$\mathbb{E}\left[C_D(\tilde{a}_1^k \cdots \tilde{a}_m^k)\right] = \mathbb{E}\left[C_D(\tilde{a}_1^k + \tau \cdots \tilde{a}_m^k + \tau)\right] = 2m\sigma^2 \tag{34}$$

where $\sigma^2$ is the variance from equation 1. Therefore, the false match $\tilde{a}_i^k + \tau$ cannot be eliminated. Now assume that we have three images $I_1$, $I_2$ and $I_3$ for displacement estimation. Similar to the case for two images, equation 28 can be modified by adding and subtracting $\tau$ to $i + a_i^k - \tilde{a}_i^k$:

$$C_D(a_1^2 \cdots a_m^2,\ \eta_1 \cdots \eta_m) =$$
$$\sum_{i=1}^{m} \left(\tilde{I}(i) - \tilde{I}(i+\tau+a_i^2-\tilde{a}_i^2-\tau) + n_1(i) - n_2(i+a_i^2)\right)^2 +$$
$$\sum_{i=1}^{m} \left(\tilde{I}(i) - \tilde{I}(i+\tau+\eta a_i^2-\eta\tilde{a}_i^2-\tau) + n_1(i) - n_3(i+\eta a_i^2)\right)^2$$

It can now be easily seen that $C_D$ has two local minima at $a_i^2 = \tilde{a}_i^2$ and at $a_i^2 = \tilde{a}_i^2 + \tau$. However unlike the case for two images, the expected value of $C_D$ at the incorrect match $a_i^2 = \tilde{a}_i^2 + \tau$ is more than its expected value at $a_i^2 = \tilde{a}_i^2$ because:

$$\mathbb{E}\left[C_D(\tilde{a}_1^k \cdots \tilde{a}_m^k)\right] = 4m\sigma^2$$

$$\mathbb{E}\left[C_D(\tilde{a}_1^k + \tau \cdots \tilde{a}_m^k + \tau)\right] = 4m\sigma^2 + \mathbb{E}\left[\sum_{i=1}^{m} (\tilde{I}(i) - \tilde{I}(i + \eta\tau))^2\right]$$

In the other words, unlike the case for two images (equation 34), the true match results in smaller average cost compared to the false match. Figure 6 shows how with two periodic images it is not possible to differentiate the true displacement ($\tilde{a}^2$, marked with a circle) from the false displacement ($\tilde{a}^2 + \tau$, marked with a cross) since $\left[I_1(i) - I_2(i + \tilde{a}^2)\right]^2$ and $\left[I_1(i) - I_2(i + \tilde{a}^2 + \tau)\right]^2$ are in average (i.e. ignoring the noise) equal. However, by adding a third image it is possible to differentiate the true displacement $\tilde{a}^2$ from the false displacement $\tilde{a}^2 + \tau$ since $\left[I_1(i) - I_2(i + \tilde{a}^2)\right]^2 + \left[I_1(i) - I_3(i + \eta_i\tilde{a}^2)\right]^2$ is in average smaller than $\left[I_1(i) - I_2(i + \tilde{a}^2 + \tau)\right]^2 + \left[I_1(i) - I_3(i + \eta_i(\tilde{a}^2 + \tau))\right]^2$.

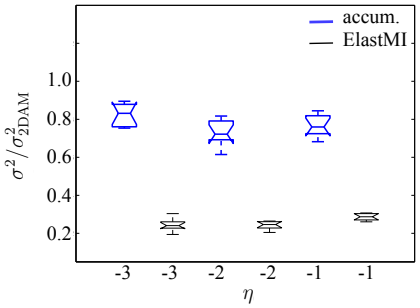


(a) axial strain

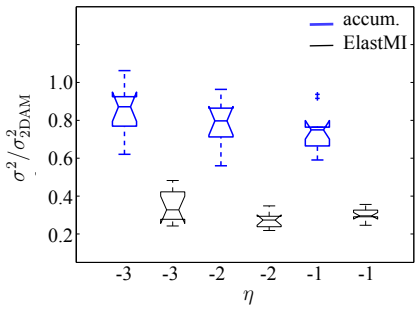


(b) lateral strain

Figure 9: Box plot of the variance of strain accumulation and ElastMI, compared to 2D AM. A ratio of smaller than 1 indicates a reduction in the variance achieved with using 3 frames.

## 5. Results

We use data from simulation, phantom experiments and patient trials to validate the performance of the ElastMI algorithm. All the ElastMI results are obtained using equation 19 with parameters defined in equations 25 and 26. The ElastMI algorithm is currently implemented in Matlab mex functions and runs in real-time on a P4 3.6GHz single core processor. In (Rivaz et al., 2011a), we proposed to estimate the strain from the displacement as following: we first applied a least square filtering in the axial direction to find an estimate for the strain. We then applied a Kalman filter in the lateral direction to remove the noise, while preventing blurring. We use the same technique here, with 50 samples in the axial direction to perform the least square fitting.

We compare ElastMI against the 2D AM strain and accumulated strain images. Two approaches are usually taken to utilize multiple images: (1) Displacements are accumulated to increase the displacement amplitudes, i.e. the Lagrangian particle tracking (e.g. for cardiac strain imaging over the cardiac cycle (Shi et al., 2008; Ma and Varghese, 2012)), and (2) strain images are averaged to reduce noise. In Lagrangian particle tracking, one should note that the location of a particle keeps changing in the image sequence, and therefore appropriate displacements must be accumulated. In ElastMI, both displacements are calculated with respect to the one reference image, i.e. $I_1$. Therefore, we do not need to perform any Lagrangian tracking and the displacements are not accumulated in ElastMI.

In all our results, we map the strain images of 2D AM, accumulated strain and ElastMI to the same range, so that they can be easily compared.

### 5.1. Simulation Results

Field II (Jensen, 1996) and ABAQUS (Providence, RI) software are used for ultrasound simulation and for finite element simulation. The specifications of the ultrasound probe and the uniform phantom are in Rivaz et al. (2011a). 8 ultrasound image frames are simulated at different compression levels from 0% to 4%, as shown in Figure 7. We set frame F7 as $I_1$ and frame F8 as $I_2$ as shown in the figure. $I_3$ is set to one of the other frames, resulting in different $\eta$ values shown in the bottom of Figure 7.

The axial and lateral strain images obtained from F7 and F8 using 2D AM are shown in Figure 8 (a). Using the three frames of F5, F7 and F8, we calculate strains between consecutive frames, add the strains, and divide it by two to have a 1% strain image similar to (a). The result is in (b). The ElastMI results using the same three frames is shown in (c). Note the SNR values shown on top of each strain image, and how it increases from 2D AM to accumulated strain to ElastMI. The axial and lateral strains in (a) to (c) have the same intensity scale (as shown in (d)) to ease comparison.

We repeat this experiment by setting $I_3$ to frames F1 through F6, and compute the ratio of the noise compared to the 2D AM strain. The result is shown in Figure 8 (e). Both ElastMI and accumulation of strain decrease the variance. However, this reduction is significantly more in ElastMI because it incorporates a powerful physical constraint into its cost function and considers all three images to estimate the displacement estimates.

Finally, we generate 10 different realizations of frame F1 in Figure 7 with 10 different simulated phantoms, and compress

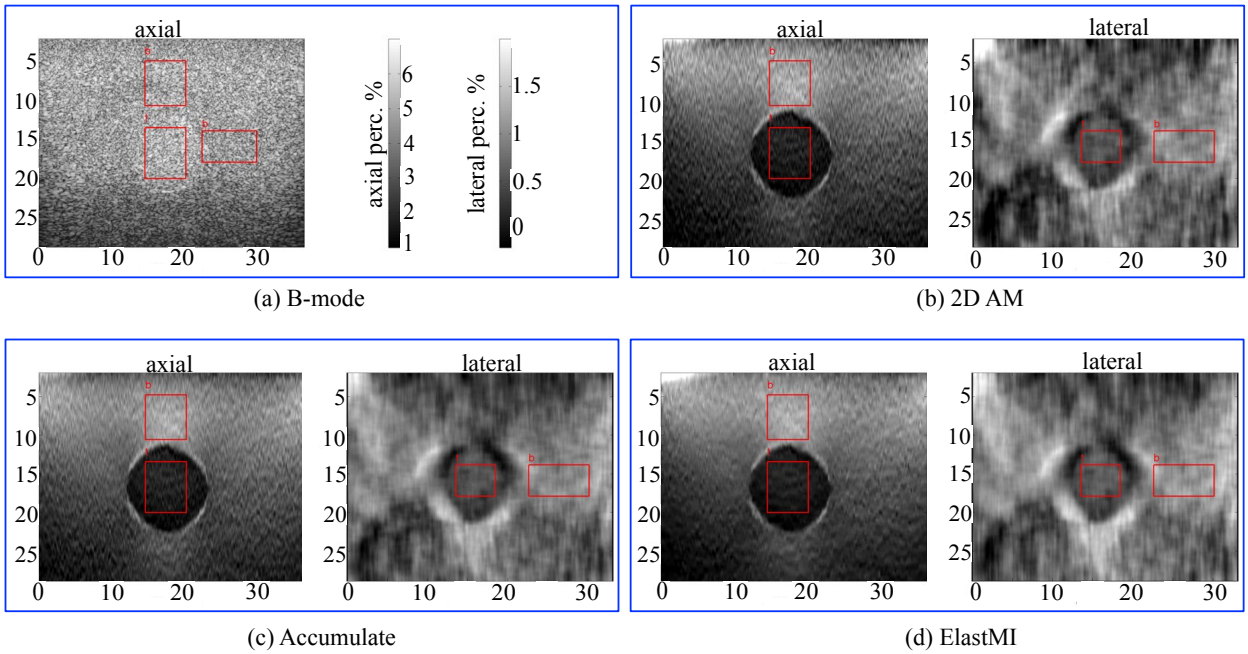


Figure 10: Axial and lateral strain images of the phantom with the target and background windows (see Table 1 for SNR and CNR values). All axes are in mm. The hard lesion is spherical and has a diameter of 1 cm. The axial and lateral strain scales are identical for all images and are shown in (a): the maximum axial and lateral strains are respectively 7% and 2%. The difference between different methods is most visible at a 2x zoom.

each phantom to obtain 10 instances of frames F3, F5, F7 and F8. We then repeat the experiment of Figure 8 (e) for each phantom. Figure 9 shows the results. Please note that we do not perform Lagrangian speckle tracking; we rather average the strain images to get the accumulated strain values. We see that using 3 images, both strain accumulation and ElastMI result in a reduction in the variance. Also, the variability in the lateral strain results in (b) is generally more than that of the axial strain images in (a). This can be attributed to the lower resolution in the lateral direction, and the lack of phase information in this direction. In both axial and lateral strains, ElastMI improves the results of strain accumulation by a statistically significant amount ($p < 0.00002$ for paired t-tests). This improvement is mainly due to imposing the physics-based prior in ElastMI.

### 5.2. *Phantom Results*

RF data is acquired from an Antares Siemens system (Issaquah, WA) at the center frequency of 6.67 MHz with a VF10-5 linear array at a sampling rate of 40 MHz. An elastography phantom (CIRS elastography phantom, Norfolk, VA) is compressed axially in two steps using a linear stage, each step 0.1 in. The Young's elasticity modulus of the background and the lesion under compression are respectively 33 kPa and 56 kPa. Three RF frames are acquired corresponding to before compression (F1), after the first compression step (F2) and after the second compression step (F3). $I_1$, $I_2$ and $I_3$ are respectively set to F2, F1 and F3. Two displacement maps, one between F1 and F2, and the second between F2 and F3 are estimated with 2D AM. They are then added to give the F1 to F3 displacement map. The unitless metrics signal to noise ratio (SNR) and contrast to noise ratio (CNR) are calculated to compare 2D AM, accumulated and ElastMI strains:

$$\mathrm{CNR} = \frac{C}{N} = \sqrt{\frac{2(\bar{s}_b - \bar{s}_t)^2}{\sigma_b^2 + \sigma_t^2}}, \quad \mathrm{SNR} = \frac{\bar{s}}{\sigma} \tag{35}$$

where $\bar{s}_t$ and $\bar{s}_b$ are the spatial strain average of the target and background, $\sigma_t^2$ and $\sigma_b^2$ are the spatial strain variance of the target and background, and $\bar{s}$ and $\sigma$ are the spatial average and variance of a window in the strain image respectively. Figure 10 shows the axial and lateral strain images along with the target and background windows used for SNR and CNR calculation. The SNR is only calculated for the background window. The results are in Table 1. In comparison with 2D AM, both accumulating strain and ElastMI improve the SNR and CNR. However, the improvement of ElastMI is significantly more which is due to the utilization of our novel mechanical prior and the EM optimization technique.

Using the same ultrasound machine and probe, we collect RF data from freehand palpation of a CIRS breast elastography phantom (CIRS, Norfolk, VA). The lesion is three times stiffer than the background. We select 10 set of ultrasound frames with 3 frames per set. We then set $I_1$ to the image with intermediate compression, and $I_2$ and $I_3$ to maximum and minimum compression. In each set, we first compute the 2D AM strains between $I_1$ and $I_2$. We then use all the three frames to compute accumulated and ElastMI strains, and compute the contrast to noise ratio between the lesion and background in each set. Figure 11 shows the results. The improvement of ElastMI over both 2D AM and strain accumulation is statistically significant

Table 1: The SNR and CNR of the strain images of Figure 10. The improvement % is w.r.t. 2D AM. The SNR is calculated for the background window. For B-mode, we calculate two values: one for the top (vertical) and another for the left (horizontal) background windows. Maximum values are in bold font.

| | B-mode | | 2D AM | | Accumulation | | ElastMI | |
|---|---|---|---|---|---|---|---|---|
| | Vert. | Horiz. | Axial | Lateral | Axial | Lateral | Axial | Lateral |
| SNR | 2.6 | 2.9 | 11.1 | 6.0 | 12.0 | 6.3 | **14.9** | **6.6** |
| SNR improv. % | - | - | 0 | 0 | 8 | 5 | **34** | **10** |
| CNR | 0.2 | 0.5 | 8.5 | 3.0 | 8.6 | 3.1 | **11.1** | **3.4** |
| CNR improv. % | - | - | 0 | 0 | 3 | 5 | **31** | **13** |

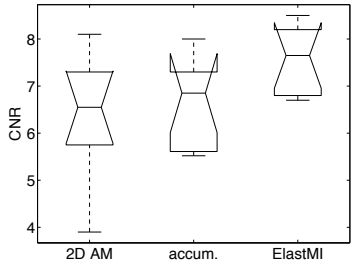


Figure 11: The CNR values of the lesion in axial strain images computed over 10 sets of ultrasound frames.

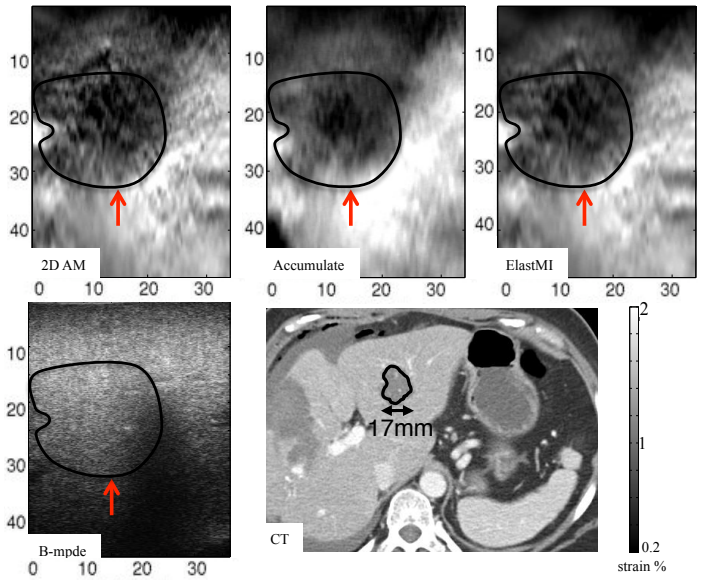


Figure 12: Strain images of the 1st *in-vivo* patient trial after ablation. The thermal lesions is delineated and pointed to by an arrow. The lateral strain images does not immediately carry anatomical information and will not be shown hereafter. All axes in mm. See also Table 2.

with $p$-values of paired t-test less than 0.002.

### *5.3. Clinical Study*

RF data is acquired from ablation therapy of three patients with liver cancer using an Antares Siemens system (Issaquah, WA) ultrasound machine. The patients underwent open surgical radiofrequency (RF) thermal ablation for primary or secondary liver cancer. All patients enrolled in the study had unresectable disease and were candidates for RF ablation following review at our institutional multidisciplinary conference. Patients with cirrhosis or suboptimal tumor location were excluded from the study. All patients provided informed consent as part of the protocol, which was approved by the institutional review board. The RF data we acquired is as follows: for the first patient only after ablation, for the second patient before and after ablation, and for the third patient before, during and after ablation. A VF10-5 linear array at the center frequency of 6.67 MHz with a sampling rate of 40 MHz is used for RF data acquisition. The ablation is administered using the RITA Model 1500 XRF generator (Rita Medical Systems, Fremont, CA). Tissue is simply compressed freehand at a frequency of approximately 1 compression per 2 sec with the ultrasound probe without any attachment and the strain images are generated offline.

The strain-stress curve of liver is approximately linear for a large strain range (Yeh et al., 2002), and therefore, the assumption that the tissue should remain linear in the three images of ElastMI is comfortably met. In addition, higher graded fibrotic liver tissue is about 4 times stiffer than lower graded fibrotic tissue (DeWall et al., 2012b), and hence, elastography imaging can potentially be used to estimate the fibrotic grade.

The strain images obtained with 2D AM, accumulation of consecutive strains and the ElastMI algorithm are shown in Figures 12, 13 and 14. Images before ablation show the tumor. Images corresponding to during ablation (second row, Figure 14) are acquired approximately 3 min after start of the ablation while the ablation device is temporarily shut down, but remains in tissue, for ultrasound data acquisition, but is still in the liver tissue. The prongs of the ablation probe are visible in the US image of the second row and are pointed to by blue arrows. Images after ablation show the ablated lesion and are acquired approximately 3 min after the ablation device is retracted from the tissue.

The severe attenuation in the B-mode image of Figure 12 has not degraded the strain images. The region with low strain in Figure 14 (d) - (f) is caused by both ablation and by the ablation probe's prongs holding the tissue, as also suggested by Varghese et al. (2004).

CNR values are calculated between target and background windows, each of size 10 mm × 10 mm. The target window is inside the tumor (before ablation) or the ablation lesion, and the background window is outside. Table 2 shows the results. ElastMI significantly improves all the CNR values. The average values for before and after ablation are shown in the last row. The average CNR over all values of this table are 5.7 for 2D AM, 5.7 for accumulating strains, and 7.3 for ElastMI. The improvements of ElastMI over both 2D AM and strain accumulation are statistically significant, with paired t-test $p$-values of

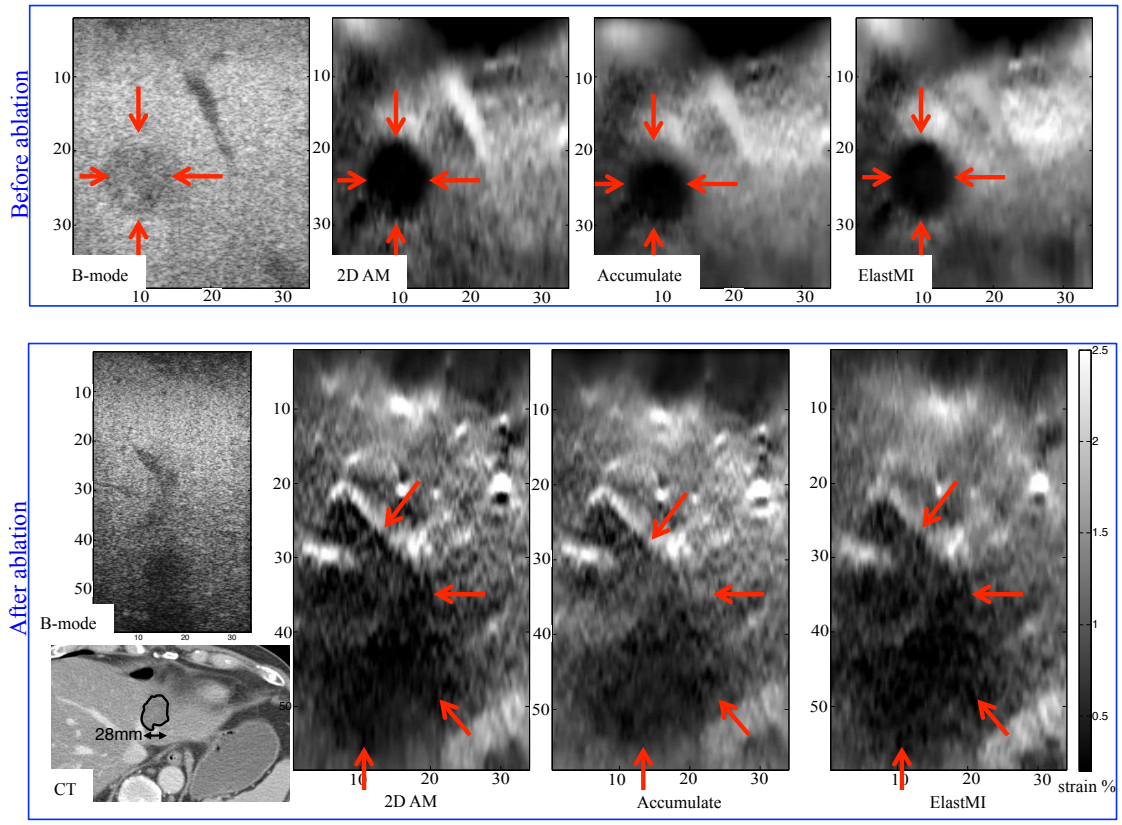


Figure 13: Strain images of the 2nd *in-vivo* patient trial corresponding to before and after ablation. The tumor in the first row and the ablation lesion in the second row are pointed to by arrows. All axes in mm. See also Table 2.

Table 2: The CNR of the strain images of Figures 12, 13 and 14. P1, P2 and P3 respectively correspond to patients 1, 2 and 3. Maximum values are in bold font.

| | Before ablation | | | During ablation | | | After ablation | | |
|---|---|---|---|---|---|---|---|---|---|
| | 2D AM | Accum. | ElastMI | 2D AM | Accum. | ElastMI | 2D AM | Accum. | ElastMI |
| P1 | - | - | - | - | - | - | 4.2 | 4.9 | **5.3** |
| P2 | 12.2 | 11.8 | **15.3** | - | - | - | 2.7 | 2.4 | **3.5** |
| P3 | 8.2 | 7.7 | **9.2** | 1.9 | 2.4 | **3.8** | 5.1 | 5.0 | **6.8** |
| average | 10.2 | 9.8 | **12.3** | 1.9 | 2.4 | **3.8** | 4.0 | 4.1 | **5.2** |

respectively 0.006 and 0.012.

Accumulating strain images generally improves the results. However, it tends to blurs sharp boundaries and lower the contrast in our experience; the tumor/ablation lesion is significantly "less dark" in Figures 12 and 13 and 12. This is an inherent result of averaging/accumulating strain images. Another reason lies in the fact that as we add consecutive strains, the chances of having incorrect displacement estimates at any part of the image increases. The ElastMI algorithm however utilizes additional physics-based priors and robust-to-outlier IRLS method to solve for displacement estimation using three images simultaneously. We see that these features enable it to continue generating low noise and sharp elasticity images in the challenging data of patient trials.

## 6. Discussions and Conclusion

In this work, we focused on utilizing three images to calculate low variance displacement fields. We first derived constraints on variation of displacement fields with time using concepts from mechanics of materials. We then proposed ElastMI, an EM based algorithm that uses these constraints. We showed that ElastMI outperforms our previous algorithm AM. We corroborated these results using simulation, phantom and *in-vivo* experiments.

The advantages of ElastMI over accumulating displacement fields of the intermediate images are as follows. First, by displacement estimation using two images only a fraction of the available information is utilized, making tracking prone to signal decorrelation and false matches. ElastMI uses all the three images in a group-wise scheme to find displacement fields. Second, the physics-based prior substantially reduces the estimation variance as shown formally and using simulation and experimental data. Finally, by accumulating displacement fields, errors are accumulated. This is in fact a well known problem of any sequential tracking or stereo system (Brown et al., 2003). Its disadvantage, however, is that it is computationally more ex-

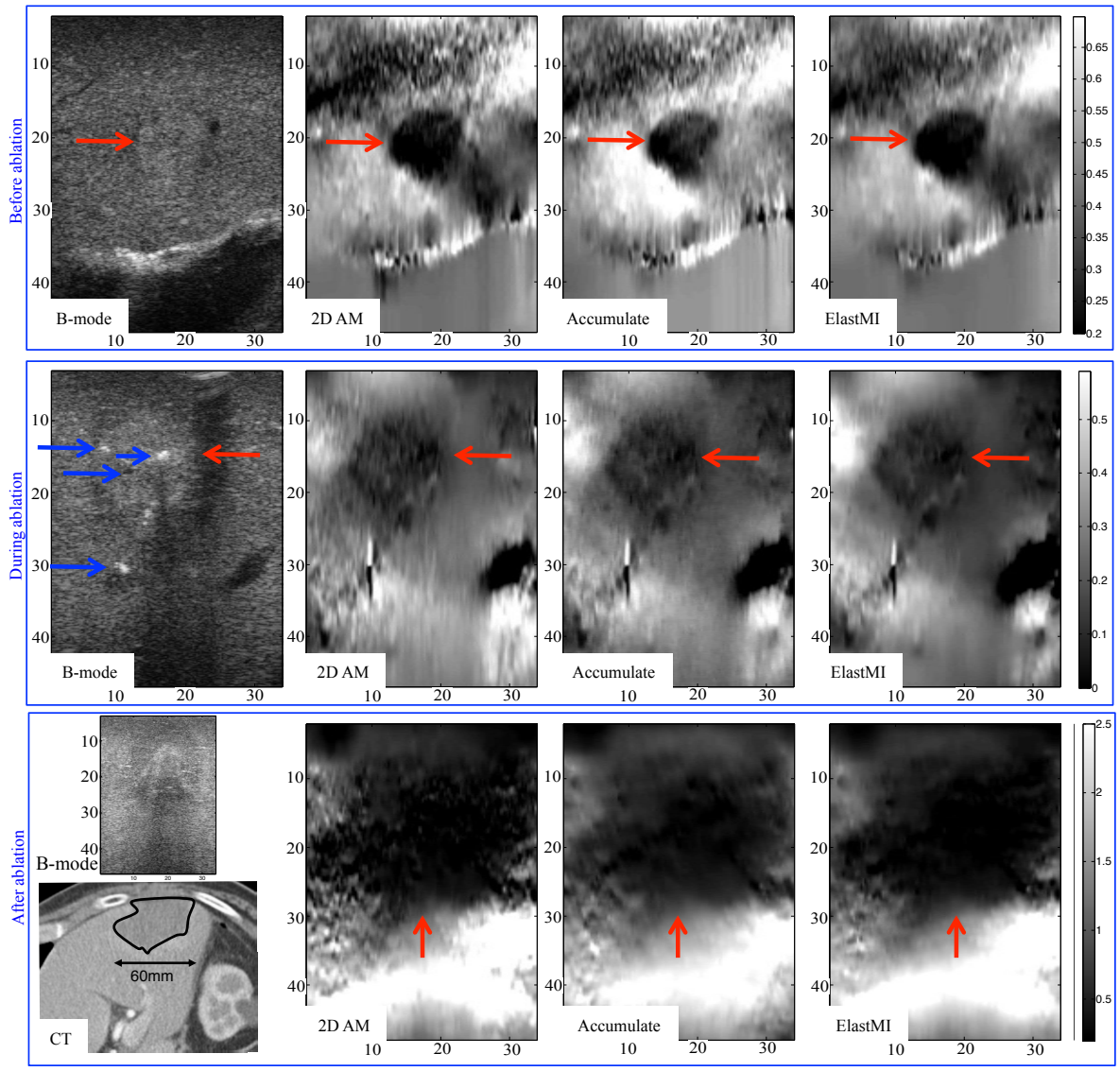


Figure 14: Strain images of the 3rd *in-vivo* patient trial corresponding to before (1st row), during (2nd row) and after (3rd row) ablation. All axes are in mm. The tumor in the top row, and the ablation lesion in second and third row are pointed to by arrows. Four prongs of the ablation probe are visible in the US image of the second row and are pointed to by arrows. CT is acquired 3 weeks after ablation. All axes in mm. See also Table 2.

pensive. In our implementation, ElastMI takes 0.2 sec to generate strain images of size $1000 \times 100$ on a single core 3.8 GHz P4 CPU, compared to 0.04 sec of 2D AM and 0.08 sec for accumulating strains.

Both ElastMI and 2D AM assume displacement fields are continuous. This assumption breaks for vascular strain imaging where the two vessel walls can move in opposite directions (Shi and Varghese, 2007; Shi et al., 2008). This issue also has been addressed in model-based elasticity reconstruction problems by assigning soft and hard constraints (Le Floc'h et al., 2009; Richards and Doyley, 2011). Therefore an interesting avenue for future work would be to relax the displacement continuity in ElastMI for image regions where 2D AM predicts high variability in the direction of displacements. Discontinuity preserving ElastMI can then be used in noninvasive vascular elastography applications (Maurice et al., 2004, 2007; Shi and Varghese, 2007; Shi et al., 2008; Hansen et al., 2009; Mercure et al., 2011; Zakaria et al., 2010; Korukonda and Doyley, 2012; Korukonda et al., 2013).

Accumulating strains significantly outperforms 2D AM in the simulation and phantom experiments. This improvement, however, mostly diminishes in the patient trials. This is mainly due to the fact that in the challenging freehand intra-operative settings, it is hard to find three "good" frames for strain computations. Therefore, one of the strain images can be noisy or blurry, and adversely affect the accumulated strain. ElastMI, however, does not suffer from this problem for two main reasons. First, the additional prior, and second, simultaneous estimation of displacement fields from three images using robust estimation methods.

We proved that for simple additive Gaussian noise, ElastMI significantly reduces the estimation noise. For ablation monitoring, however, the nature of the noise changes dramatically both with time and location because of the gas bubbles. Nevertheless, our results on the patient data shows that ElastMI performs well in the presence of such complex noise.

In the analysis of Section 3, we assumed quasi-static deformation, so that the dynamics of the continuum can be ignored. This assumption is generally valid for freehand palpation elastography. In other methods of measuring tissue elastic properties where the excitation is dynamic (Parker et al., 2005; Greenleaf et al., 2003), Kalman filters can be used to fuse the noisy displacement estimates and tissue dynamics models.

For noise analysis, we assumed additive Gaussian noise, which allowed us to analytically derive estimates for measurement variance. More accurate techniques for motion estimation have been proposed based on more realistic models of ultrasound noise (Insana et al., 2000; Maurice et al., 2007). In the future, we will consider more realistic speckle statistics, such as the models in Rivaz et al. (2007a,b, 2010).

As suggested by equation 15, the regularization can be a function of the two estimated displacement estimations. For example, $\varphi \approx 0$ or $\varphi \approx \pi$ indicate that the two estimated displacement fields are in fact similar up to a scale factor, which is what we assume in this work. However, $\varphi \approx \pm\pi/2$ indicates that the two displacements are not similar, meaning that either one of the displacement estimates is incorrect or that the tissue is highly nonlinear. Future work will exploit $\varphi$ in the regularization term (equation 15).

In the future, we will also extend the framework presented in this paper for calculating the displacement field from three images to the more general case where more than three images are utilized. Finally, direct estimation of the strain from ultrasound frames (Brusseau et al., 2008) will also be incorporated into ElastMI.


## Acknowledgment

Hassan Rivaz was supported by the DoD Predoctoral Traineeship Award and by the Advanced Simulation Fellowship from the Link Foundation. We thank anonymous reviewers for their constructive feedback, Dr. Stanislav Emelianov for his comments, Dr. Pezhman Foroughi, Ioana Fleming and Mark van Vledder for valuable discussions, and Shelby Brunke for technical support. We also thank Siemens for providing us with an Ultrasound machine with research interface, and the Hopkins Radiology department for intramural funds.


## Appendix

We now show that the additional constraint of equation 8 is critical in reducing the error in displacement estimation. Consider 3 images $I_1$, $I_2$ and $I_3$ from the set of $p$ images (Figure A-1). Let $\mathbf{d}_{12}$, $\mathbf{d}_{23}$ and $\mathbf{d}_{31}$ be the displacement between $I_1$, $I_2$, between $I_2$, $I_3$ and between $I_3$, $I_1$ (using the notation of the previous Section, $\mathbf{d}_{12} = \mathbf{d}^2$ and $\mathbf{d}_{31} = -\mathbf{d}^3$). These three displacements are not independent since $\mathbf{d}_{12} + \mathbf{d}_{23} + \mathbf{d}_{31} = 0$. The axial

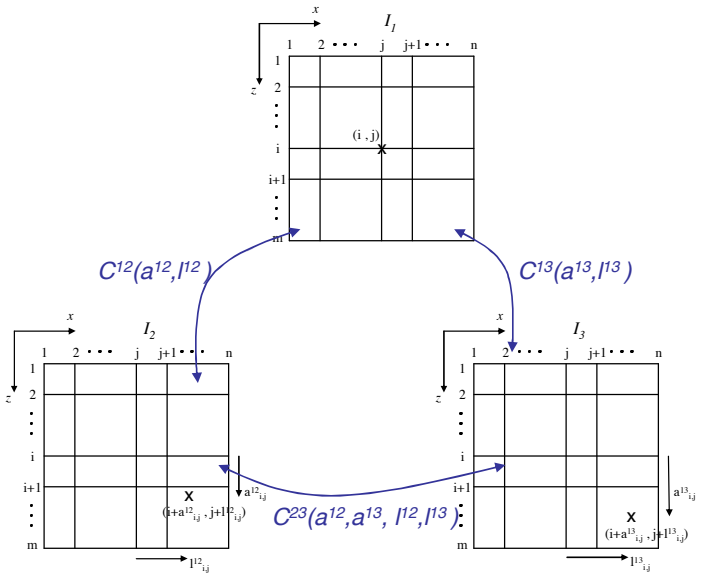


Figure A-1: Pairwise cost functions between 3 images.

component of this equation gives $a_{12} + a_{23} + a_{31} = 0$, which allows us to replace $a_{23}$ with $a_{12} = a^2$ and $a_{31} = -a^3$:

$$C_D(a_1^2 \cdots a_m^2,\ a_1^3 \cdots a_m^3) = \sum_{i=1}^{m} \left(I_1(i) - I_2(i + a_i^2)\right)^2 + \sum_{i=1}^{m} \left(I_1(i) - I_3(i + a_i^3)\right)^2 + \sum_{i=1}^{m} \left(I_2(i + a_i^2) - I_3(i + a_i^3)\right)^2 \tag{A-1}$$

where we have modified the data term of the cost function by adding the intensity similarity between each two of the three images. Note that this equation is for the displacements of any 3 images and the images need not be consecutive. Using the noise model of equation 1 and linearizing $I_2$ and $I_3$ around $i$ we have

$$\begin{aligned} &C_D(a_1^2 \cdots a_m^2,\ a_1^3 \cdots a_m^3) = \\ &\sum_{i=1}^{m} \left(-(a_i^2 - \tilde{a}_i^2) \cdot \tilde{I}'_a(i) + n_1(i) - n_2(i + a_i^2)\right)^2 + \\ &\sum_{i=1}^{m} \left(-(a_i^3 - \tilde{a}_i^3) \cdot \tilde{I}'_a(i) + n_1(i) - n_3(i + a_i^3)\right)^2 + \\ &\sum_{i=1}^{m} \left(-(a_i^2 - \tilde{a}_i^2) \cdot \tilde{I}'_a(i) + (a_i^3 - \tilde{a}_i^3) \cdot \tilde{I}'_a(i) + n_2(i + a_i^2) - n_3(i + a_i^3)\right)^2 \end{aligned} \tag{A-2}$$

The optimum value of $a_i^2$ and $a_i^3$ will minimize $C_D$. Setting $\partial C_D / \partial a_i^2 = 0$ and $\partial C_D / \partial a_i^3 = 0$ will result in a coupled 2-equations-2-unknowns linear system. Solving the set of equations will give

$$\begin{aligned} a_i^2 &= \tilde{a}_i^2 - \left[\tilde{I}'_a(i)\right]^{-1} \left(n_1(i) - n_2(i + a_i^2)\right) \\ a_i^3 &= \tilde{a}_i^3 - \left[\tilde{I}'_a(i)\right]^{-1} \left(n_1(i) - n_3(i + a_i^3)\right) \end{aligned} \tag{A-3}$$

which are the same as equation 5. Interestingly, the solution of the coupled linear system shows that $a_i^2$ does not depend on $n_3$, and similarly $a_i^3$ does not depend on $n_2$. Therefore, the implicit constraint of $a_{12} + a_{23} + a_{31} = 0$ will not reduce the noise in the displacement estimation. In the other words, the third term in the RHS of equation A-1, i.e. $\sum_{i=1}^{m} \left(I_2(i + a_i^2) - I_3(i + a_i^3)\right)^2$ will add no information to the cost function.

We have developed and implemented an algorithm that enforces the implicit constraint of this Appendix to calculate two motion fields from three images. Our simulation and experimental results showed that, compared to AM, this method has negligible impact on bias, variance, SNR and CNR of the calculated motion field and strain image as predicted by our Gaussian noise model. We do not present these results here because of space limitations.

## References


Arnal, B., Pernot, M., Tanter, M., Mar. 2011. Monitoring of thermal therapy based on shear modulus changes: Shear wave thermometry. IEEE Trans. Ultrason. Ferroelectr. Freq. Control 58 (3), 369–378.

Ayache, N., Lustman, F., . 1991. Trinocular stereo vision for robotics. IEEE Trans. Pattern Anal. Mach. Intell. 13 (1), 73–84.

Bharat, S., Varghese, T., Madsen, E., Zagzebski, J., 2008. Radio-frequency ablation electrode displacement elastography: a phantom study. Med. Phys. 35, 2432–2442.

Boctor, E., Fichtinger, G., Yeung, A., Awad, M., Taylor, R., Choti, M., Sept. 2004. Robotic strain imaging for monitoring thermal ablation of liver. Medical Image Computing & Computer Assisted Interventions, MICCAI, New York, NY, 81–88.

Brown, M., Burschka, D., Hager, G., 2003. Advances in computational stereo. IEEE Trans. Pattern Anal. Mach. Intell. 25 (8), 993–1008.

Brusseau, E., Kybic, J., Deprez, J., Basset, O., Feb. 2008. 2-D locally regularized tissue strain estimation from radio-frequency ultrasound images: Theoretical developments and results on experimental data. IEEE Trans Med Imaging 27 (2), 145–160.

Chaturvedi, P., Insana, M., Hall, T., Jan. 1998. 2-d companding for noise reduction in strain imaging. IEEE Trans. Ultrason. Ferroelectr. Freq. Control 45 (1), 179–191.

Chen, L., Housden, R., Treece, G., Gee, A., Prager, R., May 2010. A data weighting scheme for quasistatic ultrasound elasticity imaging. Univ. of Cambridge TR651.

Deprez, J., Brusseau, E., Schmitt, C., Cloutier, G., Basset, O., 2009. 3D estimation of soft biological tissue deformation from radio-frequency ultrasound volume acquisitions. Medical Image Anal. 13, 116–127.

DeWall, R., Varghese, T., Brace, C., 2012a. Visualizing ex vivo radiofrequency and microwave ablation zones using electrode vibration elastography. Med. Phys. 39, 6692–6702.

DeWall, R. J., Bharat, S., Varghese, T., Hanson, M. E., Agni, R. M., Kliewer, M. A., 2012b. Characterizing the compression-dependent viscoelastic properties of human hepatic pathologies using dynamic compression testing. Physics in medicine and biology 57 (8), 2273.

Doyley, M., Bamber, J., Fuechsel, F., Bush, N., 2001. A freehand elastographic imaging approach for clinical breast imaging: System development and performance evaluation. Ultrasound Med. Biol. 27, 1347–1357.

Emelianov, S., Erkamp, R., Lubinski, M., Skovoroda, A., O'Donnell, M., May 1998. Nonlinear tissue elasticity: Adaptive elasticity imaging for large deformations. IEEE Ultrasonics Symposium 2, 1753 – 1756.

Erkamp, R., Emelianov, S., Skovoroda, A., O'Donnell, M., 2004a. Measuring the nonlinear elastic properties of tissue-like phantoms. IEEE Trans. Ultrason. Ferroelectr. Freq. Control 51 (4), 410–419.

Erkamp, R., Emelianov, S., Skovoroda, A., O'Donnell, M., May 2004b. Nonlinear elasticity imaging: theory and phantom study. IEEE Trans. Ultrason. Ferroelectr. Freq. Control 51 (5), 532–539.

Fahey, B. J., Hsu, S. J., Wolf, P. D., Nelson, R. C., Trahey, G. E., 2006. Liver ablation guidance with acoustic radiation force impulse imaging: challenges and opportunities. Phisics in Medicine and Biology 51, 3785 – 3808.

Fellingham, L., Sommer, F., 1983. Ultrasonic characterization of tissue structure in the in vivo human liver and spleen. IEEE Trans. Sonics and Ultrasonics 31 (4), 418–428.

Foroughi, P., Rivaz, H., Fleming, I., Hager, G., Boctor, E., Sept. 2010. Tracked ultrasound elastography (true). Medical Image Computing & Computer Assisted Interventions, Beijing, China, 6–17.

Goenezen, S., Dord, J., Sink, Z., Barbone, P., Jiang, J., Hall, T., Oberai, A., 2012. Linear and nonlinear elastic modulus imaging: An application to breast cancer diagnosis. IEEE Trans. Med. Imag. 31 (8), 1628–1637.

Goldberg, S., Gazelle, G., Mueller, P., 2000. A unified approach to underlying principles, techniques, and diagnostic imaging guidance. AJR Roentgen 174, 323–331.

Greenleaf, J., Fatemi, M., Insana, M., Apr. 2003. Selected methods for imaging elastic properties of biological tissues. Annu. Rev. Biomed. Eng. 5, 57–78.

Hager, G., Belhumeur, P., Oct. 1998. Efficient region tracking with parametric models of geometry and illumination. IEEE Trans. Pattern Anal. Mach. Intell. 20 (10), 1025–1039.

Hall, T., Oberai, A., Barbone, P., Sommer, A., Gokhale, N., Goenzen, S., Jiang, J., 2009. Elastic nonlinearity imaging. IEEE EMBS, 1967–1970.

Hall, T., Oberai, A., Barbone, P., Sommer, A., Jiang, J., Gokhale, N., Goenzen, S., Oct. 2007. Imaging the elastic nonlinearity of tissues. IEEE Int. Ultrasonics Symp., in press.

Hall, T., Zhu, Y., Spalding, C., Mar 2003. In vivo real-time freehand palpation imaging. Ultrasound Med. Biol. 29, 427–435.

Hansen, H., Lopata, R., de Korte, C., 2009. Noninvasive carotid strain imaging using angular compounding at large beam steered angles: Validation in vessel phantoms. IEEE Trans. Med. Imag. 28, 872–880.

Hiltawsky, K., Kruger, M., Starke, C., Heuser, L., Ermert, H., Jensen, A., Nov. 2001. Freehand ultrasound elastography of breast lesions: Clinical results. Ultrasound Med. Biol. 27, 1461–1469.

Huber, P., 1997. Robust statistics. Wiley, New York.

Insana, M., Cook, L., Bilgen, M., Chaturvedi, P., Zhu, Y., 2000. Maximum-liklihood approach to strain imaging using ultrasound. IEEE Trans. Ultrason. Ferroelectr. Freq. Control 107 (3), 1421–1434.

Jensen, A., 1996. Field: A program for simulating ultrasound systems. Medical & Biological Engineering & Computing 34, 351–353.

Jiang, J., Brace, C., Andreano, A., DeWall, R., Rubert, N., Pavan, T., Fisher, T., Varghese, T., Lee, F., Hall, T., 2010. Ultrasound-based relative elastic modulus imaging for visualizing thermal ablation zones in a porcine model. Phys. Med. Biol. 55, 2281–2306.

Jiang, J., Hall, T., October 2006. A regularized real-time motion tracking algorithm using dynamic programming for ultrasonic strain imaging. In: IEEE Ultrasonics Symp. Vancouver, Canada, pp. 606–609.

Jiang, J., Hall, T., Sommer, A., Jun. 2006. A novel performance descriptor for ultrasonic strain imaging: a preliminary study. IEEE Trans. Ultrason. Ferroelectr. Freq. Control 53 (6), 1088–1102.

Jiang, J., Hall, T., Sommer, A., Jun. 2007. A novel image formation method for ultrasonic strain imaging. Ultrasound Med. Biol. 53 (6), 1088–1102.

Jiang, J., Varghese, T., 2009. Youngs modulus reconstruction for rf ablation electrode-induced displacement fields: a feasibility study. IEEE Trans. Med. Imaging 28, 1325–1334.

Konofagou, E., Ophir, J., 1998. A new elastographic method for estimation and imaging of lateral displacements, lateral strains, corrected axial strains and poisson's ratios in tissues. Ultrasound Med. and Biol. 24 (8), 1183–1199.

Korukonda, S., Doyley, M., 2012. Visualizing the radial and circumferential strain distribution within vessel phantoms using synthetic-aperture ultrasound elastography. IEEE Trans. UFFC 59 (8), 1639–1653.

Korukonda, S., Nayak, R., Carson, N., Schifitto, G., Dogra, V., Doyley, M., 2013. Noninvasive vascular elastography using plane-wave and sparse-array imaging. IEEE Trans. UFFC 60 (2), 332–341.

Krouskop, T., Wheeler, T., Kallel, F., Garra, B., Hall, T., 1998. The elastic moduli of breast and prostate tissues under compression. Ultras. Imag. 20, 260–274.

Le Floc'h, S., Ohayon, J., Tracqui, P., Finet, G., Gharib, A., Maurice, R., Cloutier, G., Pettigrew, R., 2009. Vulnerable atherosclerotic plaque elasticity reconstruction based on a segmentation-driven optimization procedure using strain measurements: theoretical framework. IEEE Trans. Med. Imag. 28, 1126–37.

Lubinski, M., Emelianov, S., O'Donnell, M., Jan 1999. Adaptive strain estimation using retrospective processing. IEEE Trans. Ultrason. Ferroelectr. Freq. Control 46 (1), 97–107.

Ma, C., Varghese, T., 2012. Lagrangian displacement tracking using a polar grid between endocardial and epicardial contours for cardiac strain imaging. Med. Phys. 39, 1779–92.

Maurice, R., Fromageau, J., Brusseau, E., Finet, R., Rioufol, G., Cloutier, G., Aug. 2007. On the potential of the lagrangian estimator for endovascular ultrasound elastography: In vivo human coronary artery study. Ultrasound Med. Biol. 33 (8), 1199–1205.

Maurice, R., Ohayon, J., Fretigny, Y., Bertrand, M., Soulez, G., Cloutier, G., Feb. 2004. Noninvasive vascular elastography: Theoretical framework. IEEE Trans Med Imaging 23 (2), 164–180.

McCormick, M., Rubert, N., Varghese, T., 2011. Bayesian regularization applied to ultrasound strain imaging. IEEE Trans. Biomed. Eng. 58 (6), 1612–1620.

Mercure, E., Deprez, J., Fromageau, J., Basset, O., Soulez, G., Cloutier, G., Maurice, R. L., 2011. A compensative model for the angle-dependence of motion estimates in noninvasive vascular elastography. Med. Phys. 38 (2), 727–735.

Moon, T., Nov. 1996. The expectation-maximization algorithm. IEEE Signal Proc. 13 (6), 47 – 60.

Mulligan, J., Isler, V., Daniilidis, K., . 2002. Trinocular stereo: A real-time algorithm and its evaluation. Intern. J. Comp. Vis. 47, 51–61.

Oberai, A., Gokhale, N., Goenezen, S., Barbone, P., Hall, T., Sommer, A., Jiang, J., 2009. Linear and nonlinear elasticity imaging of soft tissue in vivo: demonstration of feasibility. Phys. Med. Biol. 54, 1191–1207.

O'Donnell, M., Skovoroda, A. R., Shapo, B. M., Emelianov, S. Y., 1994. Internal displacement and strain imaging using ultrasonic speckle tracking. Ultrasonics, Ferroelectrics and Frequency Control, IEEE Transactions on 41 (3), 314–325.

Ophir, J., Alam, S., Garra, B., Kallel, F., Konofagou, E., Krouskop, T., Varghese, T., Nov. 1999. Elastography. Annu. Rev. Biomed. Eng. 213, 203–233.

Parker, K., Taylor, L., Gracewski, S., Rubens, D., May 2005. A unified view of imaging the elastic properties of tissue. J. Acoust. Soc. Amer. 117, 2705–2712.

Pellot-Barakat, C., Frouin, F., Insana, M., Herment, A., Feb. 2004. Ultrasound elastography based on multiscale estimations of regularized displacement fields. IEEE Trans Med Imaging 23 (2), 153–163.

Richards, M., Doyley, M., 2011. Investigating the impact of spatial priors on the performance of model-based ivus elastography. Phys. Med. Biol. 56, 7223–7246.

Righetti, R., Kallel, F., Stafford, J., Price, R., Krouskop, T., Hazle, J., Ophir, J., 1999. Elastographic characterization of HIFU-induced lesions in canine livers. Ultrasound Med. Biol. 25 (7), 1099–1113.

Rivaz, H., Boctor, E., Choti, M., Hager, G., April 2011a. Real-time regularized ultrasound elastography. IEEE Trans Med Imaging 30 (4), 928–945.

Rivaz, H., Boctor, E., Choti, M., Hager, G., Sept. 2011b. Ultrasound elastography using three images. Medical Image Computing & Computer Assisted Interventions Conference, MICCAI, London, UK, 371–378.

Rivaz, H., Boctor, E., Fichtinger, G., 2007a. A robust meshing and calibration approach for sensorless freehand 3d ultrasound. In: Medical Imaging. International Society for Optics and Photonics, pp. 651318–651318.

Rivaz, H., Boctor, E., Foroughi, P., Fichtinger, G., Hager, G., Oct. 2008a. Ultrasound elastography: a dynamic programming approach. IEEE Trans Med Imaging 27 (10), 1373–1377.

Rivaz, H., Fleming, I., Assumpcao, L., Fichtinger, G., Hamper, U., Choti, M., Hager, G., Boctor, E., Sept. 2008b. Ablation monitoring with elastography: 2d in-vivo and 3d ex-vivo studies. Medical Image Computing & Computer Assisted Interventions, MICCAI, New York, NY, 458–466.

Rivaz, H., Foroughi, P., Fleming, I., Zellars, R., Boctor, E., Hager, G., 2009. Tracked regularized ultrasound elastography for targeting breast radiotherapy. In: Medical Image Computing and Computer-Assisted Intervention–MICCAI 2009. Springer, pp. 507–515.

Rivaz, H., Kang, H. J., Stolka, P. J., Zellars, R., Wacker, F., Hager, G., Boctor, E., 2010. Novel reconstruction and feature exploitation techniques for sensorless freehand 3d ultrasound. In: SPIE Medical Imaging. International Society for Optics and Photonics, pp. 76291D–76291D.

Rivaz, H., Zellars, R., Hager, G., Fichtinger, G., Boctor, E., 2007b. Beam steering approach for speckle characterization and out-of-plane motion estimation in real tissue. In: Ultrasonics Symposium, 2007. IEEE. IEEE, pp. 781–784.

Shi, H., Mitchell, C., McCormick, M., Kliewer, M., Dempsey, R., Varghese, T., 2008. Preliminary in-vivo atherosclerotic carotid plaque characterization using the accumulated axial strain and relative lateral shift based strain indices. Phys. Med. Biol. 53, 6377–6394.

Shi, H., Varghese, T., 2007. Two-dimensional multi-level strain estimation for discontinuous tissue. Phys. Med. Biol. 52, 1325–1334.

Sumi, C., Feb. 2008. Regularization of tissue shear modulus reconstruction using strain variance. IEEE Trans. Ultrason. Ferroelectr. Freq. Control 55 (2), 297 – 307.

Sumi, C., Sato, K., Apr. 2008. Regularization for ultrasonic measurements of tissue displacement vector and strain tensor. IEEE Trans. Ultrason. Ferroelectr. Freq. Control 55 (4), 787 – 799.

Varghese, T., Ophir, J., Cespedes, I., 1994. Mean-scatterer spacing estimates with spectral correlation. J. Acoustic. Soc. Am. 96 (6), 3504–3515.

Varghese, T., Ophir, J., Cespedes, I., 1996. Noise reduction in elastograms using temporal stretching with multicompression averaging. Ultrasound Med. Biol. 22 (8), 1043–1052.

Varghese, T., Techavipoo, U., James, M., Zagzebski, A., Lee, F., 2004. Impact of gas bubbles generated during interstitial ablation on elastographic depiction of in vitro thermal lesions. J. Ultrasound Med. 23 (1), 535–544.

Varghese, T., Techavipoo, U., Liu, W., Zagzebski, J., Chen, Q., Frank, G., Lee Jr, F., Sept. 2003. Elastographic measurement of the area and volume of thermal lesions resulting from radiofrequency ablation: Pathologic correlation. American Journal of Roentgenology 181, 701–707.

Viola, F., Walker, W., Jan. 2005. A spline-based algorithm for continuous time-delay estimation using sampled data. IEEE Trans. Ultrason. Ferroelectr. Freq. Control 52 (1), 80–93.

Yamakawa, M., Nitta, N., Shiina, T., Matsumura, T., Tamano, S., Mitake, T., Ueno, E., May 2003. High-speed freehand tissue elasticity imaging for breast diagnosis. Jpn. J. Appl. Phys. 42 (5B), 3265–3270.

Yeh, W., Li, P., Jeng, Y., Hsu, H., Kuo, P., Li, M., Yang, P., Lee, P., 2002. Elastic modulus measurements of human liver and correlation with pathology. Ultrasound Med. Biol. 28 (4), 467–474.

Zahiri, R., Salcudean, S., Oct. 2006. Motion estimation in ultrasound images using time domain cross correlation with prior estimates. IEEE Trans. Biomed. Eng. 53 (10), 1990–2000.

Zakaria, T., Qin, Z., Maurice, R. L., 2010. Optical-flow-based b-mode elastography: Application in the hypertensive rat carotid. IEEE Trans Med. Imag. 29 (2), 570–578.